INTERNATIONAL JOURNAL FOR NUMERICAL METHODS IN FLUIDS
Int. J. Numer. Meth. Fluids 2010; **00**:1–0 *Prepared using* fldauth.cls *[Version: 2002/09/18 v1.01]*

A Numerical Scheme for Euler-Lagrange Simulation of Bubbly Flows in Complex Systems

E. Shams, J. Finn and S. V. Apte*

School of Mechanical Industrial and Manufacturing Engineering, Oregon State University, Corvallis, OR, 97331, USA.

SUMMARY

An Eulerian-Lagrangian approach is developed for the simulation of turbulent bubbly flows in complex systems. The liquid phase is treated as a continuum and the Navier-Stokes equations are solved in an unstructured grid, finite volume framework for turbulent flows. The dynamics of the disperse phase is modeled in a Lagrangian frame and includes models for motion of each individual bubble, bubble size variations due to the local pressure changes, and interactions among the bubbles and with boundaries. The bubble growth/collapse is modeled by the Rayleigh-Plesset (RP) equation. Three modeling approaches are considered: (a) one-way coupling; where the influence of the bubble on the fluid flow is neglected, (b) two-way coupling; where the momentum exchange between the fluid and the bubbles is modeled, and (c) volumetric coupling; where the volumetric displacement of the fluid by the bubble motion and the momentum-exchange are modeled. A novel adaptive time-stepping scheme based on stability analysis of the non-linear bubble dynamics equations is developed. The numerical approach is verified for various single bubble test cases to show second-order accuracy. Interactions of multiple bubbles with vortical flows are simulated to study the effectiveness of the volumetric coupling approach in predicting the flow features observed experimentally. Finally, the numerical approach is used to perform a large-eddy simulation in two configurations: (i) flow over a cavity to predict small-scale cavitation and inception, and (ii) a rising dense bubble plume in a stationary water column. Results show good predictive capability of the numerical algorithm in capturing complex flow features.

Copyright © 2010 John Wiley & Sons, Ltd.

KEY WORDS: Large-eddy Simulation, Euler-Lagrange, Bubble Dynamics, Cavitation, Discrete Bubble Model.

*Correspondence to: 204 Rogers Hall, Corvallis, OR 97331, USA. Email: sva@engr.orst.edu, Fax: 541-737-2600

Contract/grant sponsor: Office of Naval Research (Program Manager: Dr. Ki-Han Kim) and Department of Energy's National Energy Technology Laboratory; contract/grant number: N000140610697 (ONR) and 41817M4077 (DOE-NETL).

Copyright © 2010 John Wiley & Sons, Ltd.
Received
Revised

1. INTRODUCTION

Two-phase flows with phase change occur in many engineering systems. Of specific interest are two applications involving wide range of length and time scales: (a) bubbly turbulent flows in the ship boundary layers for drag reduction and (b) hydrodynamics of cavitation. These problems share common physical mechanisms of mass, momentum, and energy exchange across the interface between the two phases.

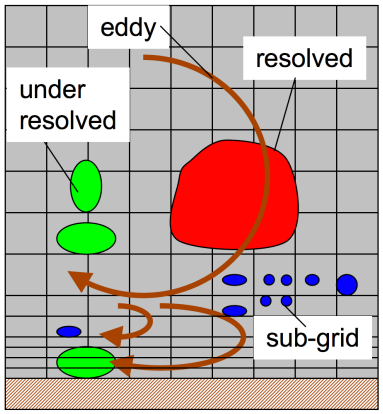

Figure 1: Schematic of fully resolved and subgrid disperse phase.

The dispersed bubbles may deform, vary in size, or coalesce and the local grid resolution may be such that the bubble is fully resolved or under-resolved in relation to the resolution of the background mesh (see Figure 1). In cavitating flows, the vapor cavity size can change dynamically and the the local grid resolution may be such that the cavity (or bubbles) are fully (or partially) resolved on the grid or completely sub-grid. Different approaches are needed to model these flow regimes accurately.

In this work, we focus on a numerical approach for the under-resolved or subgrid disperse phase (in the form of bubbles or particles). Two approaches are widely used to compute the hydrodynamics of under-resolved bubbly flows: the Euler-Euler and Euler-Lagrange. The Euler-Euler model employs the volume or ensemble averaged mass and momentum conservation equations to describe the time dependent motion of both phases [58]. In the Eulerian-Lagrangian approach, a continuum description is used for the liquid phase with discrete Lagrangian tracking of the bubbles. The bubbles are usually modeled as spherical point-particles with models for fluid-bubble interaction forces and bubble-bubble interactions [19, 10]. Such an approach has been used for turbulent bubbly-channel flows for computation of drag reduction [1], cavitation inception studies with bubble dynamics modeled using the Rayleigh-Plesset equation [24, 25]. The Euler-Lagrange approach is generally accurate in predicting the bubble dynamics and transport when all bubble trajectories relevant to a problem are tracked. This; however, also limits the capability of Euler-Lagrange approach to small number of bubbles. If the bubbles are clustered only in a small region of the computational domain that is decomposed to optimize the computation of the continuum phase fluid equations; the Lagrangian bubble tracking can lead to significant issues related

Copyright © 2010 John Wiley & Sons, Ltd.

Prepared using fldauth.cls

to load-imbalance. Recently, Darmana *et al.* [10] developed a parallelization strategy for the Euler-Lagrange bubble flow model for simulations of large number of bubbles on structured grids.

The standard approach to simulate turbulent two-phase flows with the Euler-Lagrange approach involves use of DNS, LES or RANS for the carrier phase whereas the motion of the disperse phase is modeled. The 'point-particle' (PP) assumption is commonly employed where forces on the disperse phase are computed through model coefficients. The effect of the disperse phase on the carrier phase is represented by a force applied at the *centroid* of the disperse phase. This exchange of momentum between the phases is termed as 'two-way' coupling. For applications involving dense loading of the disperse phase (for example for volume loading larger than 10^{-3} [53]), interactions among the discrete bubbles (or particles/droplets) due to collision also becomes important. Collisions together with two-way coupling interactions between the disperse and continuum phase is termed as 'four-way coupling.' When the local concentration of the disperse phase is high, the volume displaced by the disperse phase can be large. Equations using mixture theory or volume averaging have been derived for two-phase mixture [60, 15, 31] that consider the variations in the fluid void fractions in the Navier-Stokes equations for the continuum phase. In this work, we term this interaction as 'volumetric coupling.' Volumetric coupling has been commonly used for dense particulate/granular flows [50, 3] and bubble columns [57, 10, 12, 17].

In this work, we develop a finite volume based numerical technique for Euler-Lagrange simulations of bubbly flows based on the volumetric coupling. The implementation of the discretized volume-averaged two-phase equations in an unstructured grid finite volume solver [40, 39] is described in detail. The Newton's laws of motion are solved for the discrete bubble phase together with variations in bubble size due to local pressure according to the Rayleigh-Plesset equations. The accuracy of the numerical scheme and implementation of the bubble dynamics model are tested through a variety of single and multiple bubble test cases. The importance of the volumetric coupling in capturing the correct behavior of bubble-vortex interactions is shown through validations against experimental data. Capability of the numerical approach in simulating turbulent, dense bubbly flows is tested by performing large-eddy simulation of bubble-column as well as cavitation inception in a high-speed flow over cavity.

The paper is arranged as follows. The mathematical formulation for the continuum liquid phase and discrete bubble phase are described in section 2. Semi-discretized version of the liquid phase equations are presented in section 3 followed by the complete description of the numerical algorithm for the disperse and the continuum phases in section 4. Variety of verification and validation test cases are described in section 5.

2. MATHEMATICAL FORMULATION

In this work, a Euler-Lagrange approach based on the mixture-theory is used wherein the bubble-fluid interactions are captured through inter-phase momentum exchange as well as variations in local fluid void fractions. The mathematical formulation for the disperse and continuum phases is described briefly in this section.

Copyright © 2010 John Wiley & Sons, Ltd.

Prepared using fldauth.cls

2.1. Disperse Phase Equations

The motion of each individual bubble is computed by solving the equations of motion in a Lagrangian frame. The bubble size variations are modeled by the incompressible Rayleigh-Plesset equations. The position, momentum equations and bubble radius equations are given as:

$$\frac{\mathrm{d}}{\mathrm{dt}}\left(\mathbf{x}_b\right) = \mathbf{u}_b \tag{1}$$

$$m_b \frac{\mathrm{d}}{\mathrm{dt}}\left(\mathbf{u}_b\right) = \mathbf{F}_{\ell \to b} \tag{2}$$

$$\rho_\ell \left[R_b \frac{d^2 R_b}{dt^2} + \frac{3}{2}\left(\frac{dR_b}{dt}\right)^2 \right] = p_B - p_\infty - \frac{2\sigma}{R_b} - \frac{4\mu_\ell}{R_b}\frac{dR_b}{dt} \tag{3}$$

where $\mathbf{x}_b$ and $\mathbf{u}_b$ are the bubble position and velocity, m_b is the mass, $\sum \mathbf{F}_b$ is the total force acting on the bubble, R_b is the bubble radius, p_B and p_∞ are the pressures inside and outside of the bubble, σ is the surface tension coefficient, and μ_ℓ and ρ_ℓ are the liquid viscosity and densities, respectively. To estimate p_B, it is typically assumed that the bubble contains some contaminant gas which expands or contracts according to adiabatic or isothermal processes [7, 8]. The bubble inside pressure (p_B) consists of contribution from the gas pressure p_g and the vapor pressure p_v. The net force acting on each individual bubble is given as [30]:

$$\mathbf{F}_{\ell \to b} = \mathbf{F}_G + \mathbf{F}_P + \mathbf{F}_D + \mathbf{F}_L + \mathbf{F}_{AM} + \mathbf{F}_{coll} + \mathbf{F}_{\dot{R}_b} \tag{4}$$

where $\mathbf{F}_G = (\rho_b - \rho_\ell)V_b\mathbf{g}$ is the gravitational force, $\mathbf{F}_P = -V_b\nabla p$ is the pressure force due to far-field pressure gradients, $\mathbf{F}_D = -\frac{1}{2}C_D\rho_\ell\pi R_b^2|\mathbf{u}_b - \mathbf{u}_\ell|(\mathbf{u}_b - \mathbf{u}_\ell)$ is the drag force, $\mathbf{F}_L = -C_L\rho_\ell V_b(\mathbf{u}_b - \mathbf{u}_\ell) \times \nabla \times \mathbf{u}_\ell$ is the lift force, $\mathbf{F}_{AM} = -\frac{1}{2}\rho_\ell V_b\left(\frac{D\mathbf{u}_b}{Dt} - \frac{D\mathbf{u}_\ell}{Dt}\right)$ is the added mass force, and $\mathbf{F}_{coll}$ is the inter-bubble or bubble-wall collision forces. The force $\mathbf{F}_{\dot{R}_b} = -4\pi\rho_\ell R_b^2(\mathbf{u}_b - \mathbf{u}_\ell)\frac{dR_b}{dt}$ represents momentum transfer due to variations in bubble size. Here, V_b is the bubble volume, the subscripts 'b' and 'g' correspond to the bubble and the fluid, respectively. Several different models for the drag (C_D) and lift (C_L) coefficients have been used that account for bubble deformation and variations in bubble Reynolds numbers ($Re_b = \rho_\ell|\mathbf{u}_b - \mathbf{u}_\ell|2R_b/\mu_\ell$) [10]. The collision forces can be computed using the standard collision models typically used in the discrete element method and are described later.

2.2. Fluid Phase Equations

The equations for the fluid phase are obtained by making use of the mixture theory. In this formulation, the volume occupied by the bubble in a fluid control volume is accounted for by computing the local bubble (Θ_b) and fluid void fractions Θ_ℓ (such that $\Theta_b + \Theta_\ell = 1$). The continuity and momentum equations account for local changes in void fractions [31, 28]. The continuity equation is given as:

$$\frac{\partial}{\partial t}\left(\rho_\ell\Theta_\ell\right) + \bigtriangledown \cdot \left(\rho_\ell\Theta_\ell\mathbf{u}_\ell\right) = 0. \tag{5}$$

Note that no summation is implied with the subscript 'ℓ.' The local spatio-temporal variations of bubble concentration, generate a non-divergence free velocity field,

$$\nabla \cdot \mathbf{u}_\ell = -\frac{1}{\rho_\ell\Theta_\ell}\frac{D\rho_\ell\Theta_\ell}{Dt} \tag{6}$$

Copyright © 2010 John Wiley & Sons, Ltd.

Prepared using fldauth.cls

where $\frac{D}{Dt}$ is the material derivative.

Lagrangian quantities, such as bubble concentration, are interpolated to the Eulerian control volumes effectively, using the following interpolation function,

$$\Theta_b\left(\mathbf{x}_{cv}\right) = \sum_{b=1}^{N_b} V_b \mathcal{G}_\Delta\left(\mathbf{x}_{cv}, \mathbf{x}_b\right) \tag{7}$$

where $\mathcal{G}_\Delta$ is the interpolation function, N_b is the total number of bubbles, the summation is over all bubbles, $\mathbf{x_b}$ is the bubble location, and $\mathbf{x_{cv}}$ is the control volume centroid. The momentum conservation equation is given as [21]:

$$\frac{\partial}{\partial t}\left(\rho_\ell \Theta_\ell \mathbf{u}_\ell\right) + \nabla\cdot\left(\rho_\ell \Theta_\ell \mathbf{u}_\ell \mathbf{u}_\ell\right) = -\nabla\left(p\right) + \nabla\cdot\left(\Theta_\ell \mu_\ell \mathbf{D}\right) - \Theta_\ell \rho_\ell \mathbf{g} + \mathbf{f}_{b\to\ell} \tag{8}$$

where p is the dynamic pressure in the fluid phase, $\mathbf{D} = \nabla\mathbf{u}_\ell + \nabla\mathbf{u}_\ell^{\mathrm{T}}$ is the deformation tensor, and $\mathbf{f}_{b\to\ell}$ is the reaction force from the disperse phase on to the fluid phase per unit mass of fluid and is given as:

$$\mathbf{f}_{b\to\ell}\left(\mathbf{x}_{cv}\right) = \sum_{b=1}^{N_b} \mathcal{G}_\Delta\left(\mathbf{x}_{cv}, \mathbf{x}_b\right)\left(\mathbf{F}_P + \mathbf{F}_D + \mathbf{F}_L + \mathbf{F}_{AM} + \mathbf{F}_{coll} + \mathbf{F}_{\dot{R}_b}\right). \tag{9}$$

Note that the total force on the bubble consists of the pressure force, $F_P = -V_b\nabla p$. The reaction of this force onto the fluid phase results in the force density $+\Theta_b\nabla p$. This reaction term related to the pressure gradient can be combined with the pressure gradient in the momentum equation to obtain:

$$\frac{\partial}{\partial t}\left(\rho_\ell \Theta_\ell \mathbf{u}_\ell\right) + \nabla\cdot\left(\rho_\ell \Theta_\ell \mathbf{u}_\ell \mathbf{u}_\ell\right) = -\nabla\left(p\right) + \nabla\cdot\left(\Theta_\ell \mu_\ell \mathbf{D}\right) - \Theta_\ell \rho_\ell \mathbf{g} + \mathbf{f}'_{b\to\ell} + \underbrace{\Theta_b \nabla p}_{\mathbf{F_P}\ \text{Force Density}}, \tag{10}$$

where $\Theta_b\nabla p$ is the Eulerian force density obtained from the pressure force and $\mathbf{f}'_{b\to\ell}$ is the Eulerian force density constructed from the Lagrangian force on the bubbles without the pressure force (equation 9 without the pressure force, $\mathbf{F}_P$). Noting that $\Theta_b + \Theta_\ell = 1$, the above equation can be re-written in a more commonly used form by combining the first and last terms on the right-hand side of the above equation [21, 57],

$$\frac{\partial}{\partial t}\left(\rho_\ell \Theta_\ell \mathbf{u}_\ell\right) + \nabla\cdot\left(\rho_\ell \Theta_\ell \mathbf{u}_\ell \mathbf{u}_\ell\right) = -\Theta_\ell\nabla\left(p\right) + \nabla\cdot\left(\Theta_\ell \mu_\ell \mathbf{D}\right) - \Theta_\ell \rho_\ell \mathbf{g} + \mathbf{f}'_{b\to\ell}, \tag{11}$$

where $\mathbf{f}'_{b\to\ell}$ contains summation of all reaction forces in equation 9 except the pressure force. This formulation is commonly used in gas-fluidized beds [35, 10]. In the absence of any fluid velocity, but in the presence of bubbles, the pressure gradient force is then appropriately balanced by the gravity force.

For large-eddy simulation, the above equations should be spatially filtered using density-weighted Favre averaging [27]. Using the form in equation 11; however, gives rise to an unclosed term $-\overline{\Theta_\ell\nabla p}$. It is therefore advantageous to use the original form (equation 8), resulting in standard variable density LES equations [43, 39]. In this case, the reaction due to the pressure force is treated *explicitly*. For turbulent flows, the Favre averaged equations then have the same form as equation 8 with the exception that the left-hand side of the momentum equation consists of an unclosed subgrid stress term,

$$\tau_{ij} = \overline{\rho_\ell \Theta_\ell u_i u_j} - \overline{\rho_\ell \Theta_\ell u_i}\ \overline{\rho_\ell \Theta_\ell u_j}/\overline{\rho_\ell \Theta_\ell}. \tag{12}$$

Copyright © 2010 John Wiley & Sons, Ltd.

Prepared using fldauth.cls

Denoting $\rho = \rho_\ell \Theta_\ell$, Favre-averaged velocity field can be obtained as $\overline{\rho}\tilde{u}_i = \overline{\rho u_i}$. The unclosed subgrid-scale stresses can be closed by use of a Smagorinsky model with a dynamic procedure for the calculation of the model coefficient and eddy viscosity [20, 44].

$$\mu_{\rm T} = -C_S \overline{\rho_\ell \Theta_\ell} \Delta^2 {\rm S}(\tilde{u}); \quad \Delta = V_{cv}^{1/3}; \quad {\rm S}(\tilde{u}) = (\frac{1}{2} S_{ij} S_{ij})^{1/2}, \tag{13}$$

where V_{cv} is the volume of a grid cell, and the model constant C_S is obtained using the dynamic procedure and a test filter of twice the size of the control volume. The governing equation then is obtained in terms of the filtered velocity fields $\tilde{u}_i$ and the fluid viscosity μ_ℓ is changed to $\mu_{\rm eff} = \mu_\ell + \mu_T$ accounting for the eddy viscosity.

3. DISCRETIZATION OF FLUID PHASE EQUATIONS

The numerical scheme for unstructured, arbitrary shaped elements [39] is modified to take into account the fluid void fraction. The changes in local fluid volume fractions requires solution of a *variable density* flow field as opposed to the constant density, incompressible flows studied in [5, 40]. The steps in solving the coupled fluid-particle equations are given below. A semi-implicit scheme is used for the fluid solver, however, the interphase momentum exchange terms are treated explicitly.

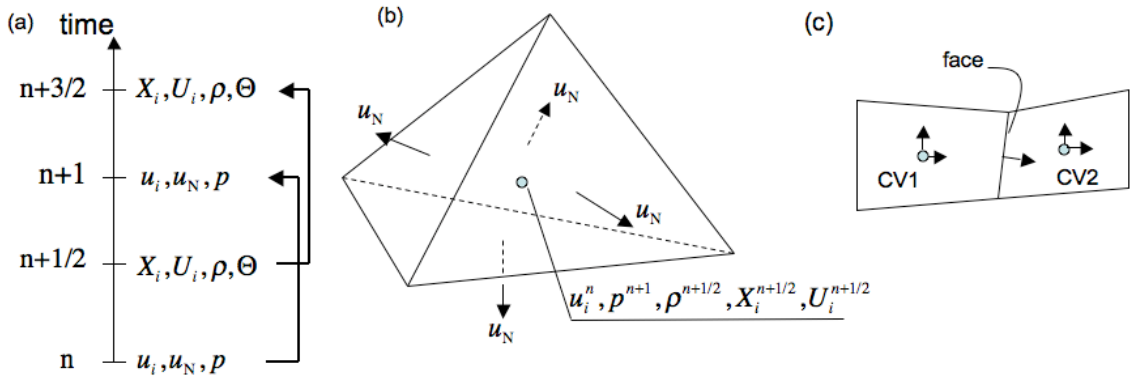

Figure 2: Schematic of the grid stencil: (a) time staggering of variables, (b) velocity (u_i) and pressure fields (p) are colocated at the control volume center, $u_{\rm N}$ is the face-normal velocity, (c) control volume and face connectivity.

Figure 2 shows the schematic of variable storage in time and space. The dispersed phase positions, density, pressure and volume fractions are staggered in time with respect to the fluid and particle velocity fields, u_i and U_i, respectively. All variables are stored at the control volume (cv) center with the exception of the face-normal velocity $u_{\rm N}$, located at the face centers. The face-normal velocity is used to enforce continuity equation. Capital letters are used to denote disperse phase. The time-staggering is done so that the variables are located most conveniently for the time-advancement scheme. We follow the collocated spatial arrangement for velocity and pressure field as has been used by [33], [40], [39]. The main reason to use this arrangement

Copyright © 2010 John Wiley & Sons, Ltd.

Prepared using fldauth.cls

as opposed to spatial-staggering is its easy application to unstructured grids and/or adaptive mesh refinement. Accordingly, the dispersed phase positions (X_i), density (ρ), volume fraction (Θ), and viscosity (μ) are located at time level $t^{n+1/2}$ and $t^{n+3/2}$ whereas the fluid velocity (u_i, $u_{\rm N}$) and the dispersed phase velocity (U_i), and the pressure (p) are located at time level t^n and t^{n+1}. This makes the discretization symmetric in time, a feature important to obtain good conservation properties of the numerical scheme as emphasized and used by Pierce and Moin [47] for low-Mach number, reactive flows.

Using these variable locations, integrating the governing equations over the control volume and applying Gauss' divergence theorem to transport volume integrals to surface integrals wherever possible, the discrete governing equations are derived. Accordingly, the continuity equation is

$$\frac{\rho_{\rm cv}^{n+3/2} - \rho_{\rm cv}^{n+1/2}}{\Delta t} + \frac{1}{V_{\rm cv}} \sum_{\text{faces of cv}} \rho_{\rm cv}^{n+1} u_{\rm N}^{n+1} A_{\rm face} = 0, \tag{14}$$

where $\rho_{\rm cv} = \rho_{\ell,{\rm cv}} \Theta_{\ell,{\rm cv}}$ is the density at the CV-center, Δt is the flow solver time-step, $V_{\rm cv}$ is the volume of the CV, $A_{\rm face}$ is the area of the face of a CV, $u_{\rm N}$ is the face-normal velocity, and $\rho_{\rm face}$ is the density at face of a CV. The density at the face can be readily obtained by using the arithmetic averages of the densities of the adjacent CVs (see figure 2), that is, $\rho_{\rm face} = \frac{1}{2}(\rho_{\rm cv1} + \rho_{\rm cv2})$. However, for the present co-located grid finite volume scheme the critical difference between the density and the face-normal velocity is that, the face-normal velocity $u_{\rm N}$ is obtained through a projection scheme rather than interpolation. Furthermore, the density at time level t^{n+1} is also obtained from interpolation, $\rho_{\rm face}^{n+1} = (\rho_{\rm face}^{n+3/2} + \rho_{\rm face}^{n+1/3})/2$.

The discrete momentum equation for the i^{th} component of velocity can be written as

$$\begin{aligned} \frac{g_{i,{\rm cv}}^{n+1} - g_{i,{\rm cv}}^{n}}{\Delta t} + \frac{1}{V_{\rm cv}} \sum_{\text{faces of cv}} g_{i,{\rm face}}^{n+1/2} u_{\rm N}^{n+1/2} A_{\rm face} \quad &= \quad -\frac{\partial}{\partial x_i} p_{\rm cv}^{n+1} + \\ \frac{1}{V_{\rm cv}} \sum_{\text{faces of cv}} (\tau_{ij})_{\rm face}^{n+1/2} {\rm N}_{j,{\rm face}} A_{\rm face} + f_{i,{\rm cv}}^{n+1/2}, \end{aligned} \tag{15}$$

where $g_i = \rho u_i$ represents the momentum in the i^{th} direction, $(\tau_{ij})_{\rm face}$ is the viscous stress at the faces of control volume, and ${\rm N}_{j,{\rm face}}$ represents the components of the outward face-normal. Similarly to the face density ($\rho_{\rm face}$), the velocity field ($u_{i,{\rm face}}$), and the momentum $\rho u_{i,{\rm face}}$ at the faces are obtained using arithmetic averages of the corresponding fields at two control volumes associated with the face. The values at time level $t^{n+1/2}$ are obtained by time-averaging. The interface coupling force is represented by $f_{i,{\rm cv}}$. The pressure field $p_{\rm cv}^{n+1}$ is unknown and is obtained using the best available guess at the current iteration. This gets updated during the solution of the pressure Poisson equation. The above discretization is implicit and thus the time-steps are not limited by viscous stability limits. The use of symmetric centered differences in space and time makes the algorithm second order on uniform Cartesian grids. The above formulation can also handle variations in the fluid density (due to say temperature variations in a gaseous fluid) by relating the fluid density ρ_ℓ to state variables through proper equation of state.

Copyright © 2010 John Wiley & Sons, Ltd.

Prepared using fldauth.cls

4. NUMERICAL ALGORITHM

The coupled ordinary-differential equations for the subgrid dispersed phase are solved first. The fluid-phase equations are solved using a pressure-based scheme for variable-density (due to void fraction variations), low-Mach number formulation as described below. The interaction forces between the two phases are treated explicitly.

4.1. Disperse-Phase Solution:

The equations for position and velocity of the dispersed phase are solved using explicit time advancing. This involves interpolation of the fluid velocity (for drag force calculation), pressure gradient (for pressure force), and vorticity (for lift force) to the disperse phase location. The interpolation is performed using the same Eulerian-Lagrangian interpolation kernel used for computation of the void fraction as described below.

4.1.1. Collision Force: The collision force is computed using a discrete element model of Cundall & Strack [9]. Note that other event-based collision models can be used (such as those proposed by Darmana *et al.* [10]) and implemented. Accordingly, the force F_{pj} on bubble p due to collision with bubble j is given by

$$F_{\text{coll}}^{pj} = \begin{cases} 0 & \text{for } d^{pj} \geq (R_p + R_j + \alpha) \\ \left(k_c \delta_{pj}^{3/2} - \eta_c (\mathbf{u}_p - \mathbf{u}_j) \cdot \mathbf{n}_{pj} \right) \mathbf{n}_{pj} & \text{for } d^{pj} < (R_p + R_j + \alpha) \end{cases} \tag{16}$$

where d^{pj} is the distance between the centers of the p^{th} and j^{th} bubbles, $\mathbf{n}_{pj}$ is the unit vector from the center of bubble j to that of bubble p, α is the force range, k_c the stiffness parameter, and η_c the damping parameter, R_p and R_j are the equivalent radii of bubbles, $\delta^{pj} = (R_p + R_j + \alpha) - d^{pj}$. Also, in order to conserve the binary collision forces, $F_{\text{coll}}^{jp} = -F_{\text{coll}}^{pj}$. Tsuji *et al.* [56] used the following expressions to compute the damping parameter

$$\eta_c = 2\alpha \sqrt{\frac{m_p k_c}{1 + \alpha^2}}; \qquad \alpha = -\ln(e/\pi) \tag{17}$$

where e is the coefficient of restitution, m_p is the mass of the bubble (p). Similarly, the collision force ((F_{coll}^{pw}) between the bubble (p) and the wall (w) is given

$$F_{\text{coll}}^{pw} = \begin{cases} 0 & \text{for } \ d^{pw} \geq (R_p + \alpha) \\ \left(k_c \delta_{pw}^{3/2} - \eta_c (\mathbf{u}_p) \cdot \mathbf{n}_{pw} \right) \mathbf{n}_{pw} & \text{for } d^{pw} < (R_p + \alpha) \end{cases} \tag{18}$$

where d^{pw} is the distance between the bubble center and the wall, and $\mathbf{n}_{pw}$ is the unit vector from the wall to the center of the parcel.

To compute the collision force on a bubble, potential collision partners need to be identified from surrounding bubbles. If there are N bubbles in the domain, computation of binary collision is an N^2 problem, significantly hampering the time required for collision calculations per time-step in dense systems. Several approaches to in forming a list of bubbles for potential collision partner have been used to reduce this computing time involving formation of linked-lists [22] and Verlet lists [2]. In the present work, a simple node-based linked list of bubbles is formed. First, all bubbles are located onto the computational mesh that is partitioned for parallel processing using the search algorithms [5]. Knowing the control volume in which the

Copyright © 2010 John Wiley & Sons, Ltd.

Prepared using fldauth.cls

bubble lies, each bubble is assigned to one of the nodes (or vertex) of the control volume depending upon its proximity to the node. Sine a node (or vertex) can share several control volumes a list (using compact storage format) of all bubbles associated with a node is created. Note that the grid partitioning algorithm (METIS [32]) uses partitions the grid along the edges of the control volume. Thus nodes on the boundary of a processor can share control volumes that are part of different processors. A communication across the processors is needed to form the node-based linked list of bubbles. Figure 3 indicates a schematic of the bubble list creation.

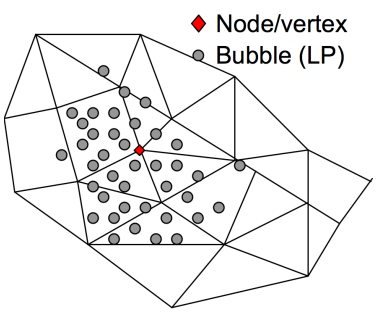


```
Create a linked list of all bubbles (lpono) associated with a node/vertex
(1:n_node) of a control volume (i_cv)
for ib = 1, n_bubble
    get i_cv for bubble ib (known vicinity algorithm)
    find nno_f and non_l (first and last node number) for the icv
    for non = non_f, non_l
        get the node index i_node corresponding to
        get all bubbles belonging to i_node (from lpono(i_node))
        use bubbles for binary collision with ib
    end
end
```

Figure 3: Creation of list of bubbles associated with a node/vertex.

Once this list is formed, the collision partner for a given bubble (ib) is chosen as follows:

1. Identify the control volume (i_{cv}) in which the bubble lies.
2. Identify the nodes of associated with the control volume.
3. For each node of the control volume, loop over the list of bubbles associated with the node.
4. Check for potential collision of the bubble with neighboring bubbles and compute the collision force.

This procedure, effectively restricts the number of bubbles that are searched in order to obtain a binary collision partner. However, if the bubbles are present only on few processors, load-imbalance can still occur. Advanced domain decomposition strategies are needed to further improve the performance of the collision algorithm. In the present work, the above approach was deemed sufficient for computation of bubbles on the order of 10^5.

4.1.2. Solution to Rayleigh-Plesset Equation: The bubble dynamics is modeled by Rayleigh-Plesset equation [48]. In this section we provide details of an adaptive time stepping method for the solution of Rayleigh-Plesset equation based on the stability criteria of the highly non-linear second-order ordinary differential equation. Solution to the Rayleigh-Plesset equation can involve sharp variations in (R_b) near the collapse region of the bubble. It shows singular behavior when the bubble radius tends to zero. An ideal numerical scheme should be able to handle the rebound behavior of the bubble after it collapses; however, the solution may become unstable if the time step used is not chosen properly. Use of a simple explicit scheme with very small time-step can be prohibitively expensive even for a single bubble computation. An adaptive time-stepping strategy is necessary such that the bubble collapse and rapid expansion regions utilize small time-steps, but a much larger time-step can be used for relatively slow

Copyright © 2010 John Wiley & Sons, Ltd.

Prepared using fldauth.cls

variations in bubble radius. So we adaptively resize the time step used for the solution of the disperse phase based on the stability threshold as derived below. Adaptive time-step refinement has been used for the solution of Rayleigh-Plesset equation [1]. However, in the present approach a new stability-analysis based adaptivity criterion is developed. This approach will be shown to be robust for rapid changes in pressure in turbulent cavitating flows.

The equation for bubble radius variations (equation 3) can be cast into two first order ODEs [1]:

$$\frac{dR_b}{dt} = y; \quad \frac{dy}{dt} = -\frac{3y^2}{2R_b} + \frac{p_B - p_\infty - 2\sigma/R_b}{\rho_\ell R_b} - \frac{4\mu_\ell y}{\rho_\ell R_b^2}. \tag{19}$$

This can be written in a matrix notation $[X]' = [F]$ where $[X]$ and $[F]$ are 2×1 matrices defined below:

$$[X] = \begin{bmatrix} R_b \\ y \end{bmatrix}; \quad [F] = \begin{bmatrix} y \\ -\frac{3y^2}{2R_b} + \frac{p_B - p_\infty - 2\sigma/R_b}{\rho_\ell R_b} - \frac{4\mu_\ell y}{\rho_\ell R_b^2} \end{bmatrix}. \tag{20}$$

Following the above notation, a simple first-order blended Euler scheme can be derived:

$$[X]^{k+1} = [X]^k + h\left(\theta[F]^k + (1-\theta)[F]^{k+1}\right), \tag{21}$$

where h is the step size, k and $k+1$ denote the current and next time levels, respectively. The blending parameter (θ) can be changed between 0 and 1 to change the scheme from fully implicit backward Euler to fully explicit forward Euler method.

In presence of large variations in the outside pressure (P_∞), the bubble radius R_b and its time derivative $\dot{R_b}$ can change rapidly, which may give rise to numerical instability. Using the notion of modified ODE for the stability analysis [42], one can derive the general stability criteria for any system of first order ODE. Defining the Jacobian matrix $[J] = \partial[F]/\partial[X]$ which is approximated at an old time level, the differential equation can be written as

$$\frac{[X]^{k+1} - [X]^k}{h} = \theta[J]^k[X]^k + (1-\theta)[J]^k[X]^{k+1}. \tag{22}$$

Rearranging this can be written in terms of the amplification matrix ($[A]$) as,

$$[X]^{k+1} = [A]^k[X]^k, \tag{23}$$

where $[A]^k = \{1 - h(1-\theta)[J]^k\}^{-1}(1 + h\theta[J])$. This equation can be diagonalized to give

$$[Z]^{k+1} = [\lambda]^k[Z]^k \tag{24}$$

where λ is the matrix of eigenvalues λ_1 and λ_2 associated with R_b and dR_b/dt, respectively. The solution of equation 24 is of the form:

$$Z_1^k = e^{\lambda_1} Z_1^0; \quad Z_2^k = e^{\lambda_2} Z_2^0. \tag{25}$$

The adaptive time-stepping strategy here is therefore, to keep the magnitude of λ_1 and λ_2 close to unity. The magnitude of the eigenvalues is adjusted by resizing the time step h at each subcycling time steps for the solution of Rayleigh-Plesset equation. Different steps in time step calculation are explained below:

Copyright © 2010 John Wiley & Sons, Ltd.

Prepared using fldauth.cls

- **Step 1:** With $f_1 = y = \frac{dR_b}{dt}$ and $f_2 = \frac{-3y^2}{2R_b} + \frac{(P_B - P_\infty - 2\sigma/R_b)}{\rho_\ell R_b} - \frac{4\mu_\ell y}{\rho_\ell R_b^2}$, calculate the Jacobian matrix

$$[J] = \frac{\partial[F]}{\partial[X]} = \begin{bmatrix} \frac{\partial f_1}{\partial x_1} & \frac{\partial f_1}{\partial x_2} \\ \frac{\partial f_2}{\partial x_1} & \frac{\partial f_2}{\partial x_2} \end{bmatrix} = \begin{bmatrix} 0 & 1 \\ \frac{3}{2}\left(\frac{y}{R_b}\right)^2 - \frac{P_B - P_\infty}{\rho_\ell R_b^2} + \frac{4\sigma}{\rho_\ell R_b^3} + \frac{8\mu_\ell y}{\rho_\ell R_b^3} & -\frac{3y}{R_b} - \frac{4\mu_\ell}{\rho_\ell R_b^2} \end{bmatrix} \tag{26}$$

- **Step 2:** Calculate matrix $[A]$ and its eigenvalues λ_1 and λ_2. Then calculate their deviation from unity, $\delta = \max(abs(\lambda_1 - 1), abs(\lambda_2 - 1))$.
- **Step 3:** Compare δ to δ_{max} and resize h accordingly. Here, δ_{max} represents the critical value in this calculation. It should be as large as possible to achieve minimum number of time steps in the computation. In the test cases presented in following sections, δ_{max} was set to 5%. Different time step resizing strategies are possible; to modify the time-step:
  - **3.1:** if h is small or $\delta < \delta_{max}$ then $h' = 2 \times h$.
    Keep multiplying by two until $\delta(h) < \delta_{max} < \delta(h')$.
  - **3.2:** if h is large or $\delta_{max} < \delta$ then $h' = 0.5 \times h$.
    Keep multiplying by 0.5 until $\delta(h') < \delta_{max} < \delta(h)$.
  - **3.3:** Once δ_{max} is between $\delta(h)$ and $\delta(h')$, average h and h' ($h_{new} = 0.5 \times (h + h')$).
    Repeat the above calculations with the averaged value until $\delta(h_{new})$ is close enough to δ_{max}.

The new time-step obtained above is based on stable solution of the Rayleigh-Plesset equation and is denoted as Δt_{RP}. This approach is found to be very effective even in the case of rapid and large pressure variations as shown in the validation cases in the following sections.

4.1.3. Subcyling and Adaptive Time Step Selection: Once all the forces are know for each bubble, the position and velocity field are advanced using an explicit Euler scheme from $t^{n+1/2}$ to $t^{n+3/2}$. It is important to note that the time-scales associated with subgrid bubbles can be vastly different from those of the flow solver time step ($\Delta t = t^{n+3/2} - t^{n+1/2}$). Thus, the time step used for integration of the dispersed phase equations can be different than the flow solver time step. The time scales associated with the bubble motion can be characterized by looking at the various forces acting on the bubbles. For example, the expression for the acceleration due to drag force (F_D/m_b) can be rearranged to provide the particle relaxation time-scale:

$$\frac{F_D}{m_b} = -\frac{(u_b - u_\ell)}{\tau_b}; \qquad \tau_b^{-1} = \frac{3}{4} C_D \frac{\rho_\ell}{\rho_b} \frac{|u_b - u_\ell|}{d_b}. \tag{27}$$

Likewise the time-scale associated with the lift force is proportional to the vorticity magnitude; $\tau_L^{-1} = C_L |\nabla \times \mathbf{u}_\ell|$. The collision force also is constrained by a time-scale which depends on the collision model and the parameters used. For the collision model described above, Cundall & Strack [9] propose a time step restriction given as $\Delta t_{\text{coll}} \leq \sqrt{m_b/k_c}$. Finally, in the presence of large variations in fluid pressure, the time-scale restrictions based on the Rayleigh-Plesset equations (Δt_{RP}) can be obtained from the stability analysis described above.

Since we use explicit time-stepping, the time step (Δt_{bub}) used for advancing the disperse phase equations should be comparable to the smallest time-scales governing their dynamics. Accordingly, for each flow-solver time-step (Δt), the time step used for bubble dynamics is obtained as follows:

Copyright © 2010 John Wiley & Sons, Ltd.

Prepared using fldauth.cls

$$\Delta t_{\text{bub}} = \min\left(\frac{\Delta t}{3}, \tau_b, \tau_L, \tau_{\text{coll}}, \Delta t_{\text{RP}}\right). \tag{28}$$

If the other time-scales are larger than the flow-solver time-scale, this expression makes $\Delta t_{\text{bub}} = \Delta t/3$. The factor 3 is used to get better accuracy than first-order Euler. Since Δt_{bub} can be smaller than flow solver time-step (Δt), a sub-cycling procedure may be necessary. The bubble dynamics equations are solved repeatedly until we reach one flow solver time step (Δt). The bubble dynamics equations are updated using explicit Euler scheme; the bubbles located using search algorithms for unstructured grids [5] are duly transferred across processors as their positions are updated. During this sub-cycling process, it is assumed that the fluid flow quantities do not change significantly similar to a quasi-steady assumption. In addition, typically for time-resolved simulations (such as large-eddy simulation), it is necessary to use the flow solver time-step such that the convective CFL number is less than unity. Under these conditions, in most applications, the bubbles may not move significantly during one time-step. Hence, an actual update of the neighbor list for collision partners can only be done once per flow solver time-step.

4.1.4. Interpolation Operator for Lagrangian-Eulerian Mapping: In the simulation of a coupled liquid and bubble system, mapping data from Eulerian framework (liquid phase) to Lagrangian framework (bubble/particle phase) is necessary. In the Lagrangian calculation, data sets such as flow velocity, pressure, acceleration, etc., are needed for the bubble/particle motion. On the other hand, reaction forces acting on liquid phase and bubble volume fraction are needed to be mapped into Eulerian framework.

The interpolation function should be smooth and conserve the transferred variable [34]. In an orthogonal structured computational grid, linear or bilinear interpolation technique can be applied, depending on the level of accuracy needed. Snider *et al.* [50] used a trilinear interpolation technique in a staggered grid computation. McDermott and Pope [41] have recently proposed the Parabolic Edge Reconstruction Method (PERM) for continuous velocity field reconstruction in the subgrid level. Kernel-based interpolation techniques, typical of particle methods, can be easily applied to complex and unstructured grids. Different interpolation kernels using polynomial [12, 10] or exponential [16, 4] function formulation have been used. Gaussian kernel provides quadrature spectral accuracy, provided that the interpolation is being performed over a region much larger than the kernel width [16], otherwise the accuracy reduces to second order. They do not have a compact support, but are smooth, accurate and easy for use on unstructured grids.

The Gaussian interpolation function is given by

$$\mathcal{G}_\sigma(\mathbf{x}, \mathbf{x}_b) = \frac{1}{\sigma\sqrt{(2\pi)})^3} \exp(\left[-\frac{\sum_{k=1}^{3}(x_k - x_{b,k})^2}{2\sigma^2}\right], \tag{29}$$

where σ is the kernel width, x_k and $x_{b,k}$ denote the available data point on the grid and the bubble location, respectively. In order to enforce mass conservation, the kernel function is normalized over the volume of integration by

$$\int_{V_{cv}} \mathcal{G}_\sigma(\mathbf{x}_{cv}, \mathbf{x}_b) dV = 1. \tag{30}$$

Copyright © 2010 John Wiley & Sons, Ltd.

Prepared using fldauth.cls

Using the above kernel, volume fraction of the liquid can be calculated as

$$\Theta_\ell = 1 - \frac{\sum_{i=1}^{n_b} V_b \mathcal{G}_\sigma}{V_{cv}}. \tag{31}$$

4.2. Fluid-Phase Solution:

The fluid flow solver is based on a co-located grid finite volume scheme for arbitrary shaped unstrcutured grids [39, 43]. The main steps of the solver are described below.

- **Step 1:** Advance the bubble positions, velocities, and radii using the adaptive time-stepping algorithm described above. Compute the void fraction field at the new bubble locations using the Lagrangian-Eulerian interpolation kernel and set the density $\rho = \rho_\ell \Theta_\ell$. The pressure seen by the bubble (p_∞ in the Rayleigh-Plesset equation) is basically obtained as follows: we first interpolate the pressure gradient from the $faces$ of a control volume to the cv centers using a least-squares interpolation consistent with the pressure reconstruction (Step 6 below). The pressure field at any point within the cv centers is then obtained by using a linear interpolation in space as well as linear interpolation in time. This preserves the continuity of the pressure field from one cell to another.
- **Step 2:** Advance the fluid momentum equations using the fractional step algorithm, with the interphase force, f_i, treated explicitly (the subscript ℓ for fluid phase is dropped for simplicity).

$$\frac{\rho_{\rm cv}^{n+1} u_i^* - \rho_{\rm cv}^n u_i^n}{\Delta t} + \frac{1}{2V_{\rm cv}} \sum_{\text{faces of cv}} \left[\rho_{\rm face}^{n+1} u_{i,\rm face}^* + \rho_{\rm face}^n u_{i,\rm face}^n\right] u_{\rm N}^{n+1/2} A_{\rm face} =$$
$$-\frac{\delta p}{\delta x_i}^n + \frac{1}{2V_{\rm cv}} \sum_{\text{faces of cv}} \mu_{\rm face}^* \left(\frac{\partial u_{i,\rm face}^*}{\partial x_j} + \frac{\partial u_{j,\rm face}^n}{\partial x_i}\right) A_{\rm face} + f_i^{n+1/2}, \tag{32}$$

  where N is the face-normal component, and $A_{\rm face}$ is the face area. The density fields at faces are obtained using simple arithmetic averages of density at adjacent CVs. Here the fluid viscosity is given as $\mu_{\rm face}^* = \Theta_{\ell,\rm face} \mu_{\rm eff,face}$ where $\mu_{\rm eff}$ is the summation of the dynamic viscosity and eddy viscosity obtained from the dynamic Smagorinsky model. The pressure gradient at the CV centers in the above equation is at the old time-level and is obtained as described below. The reaction force $f_i^{n+1/2}$ is obtained through Lagrangian-Eulerian interpolation and consists of the pressure force on the disperse phase. In the above step, the viscous terms are treated implicitly, the three equations for the velocity components at the CV centers are solved using iterative scheme such as Gauss-Seidel.
- **Step 3:** Remove the old pressure gradient to obtain the velocity field, $\widehat{u}_i$:

$$\frac{\rho_{\rm cv}^{n+1} \widehat{u}_i - \rho_{\rm cv}^{n+1} u_i^*}{\Delta t} = +\frac{\delta p}{\delta x_i}^n \tag{33}$$

- **Step 4:** Interpolate the velocity fields to the faces of the control volumes and consider the corrector step:

$$\frac{\rho_{\rm face}^{n+1} u_{\rm N}^{n+1} - \rho_{\rm face}^{n+1} \widehat{u}_{\rm N}}{\Delta t} = -\frac{\delta p}{\delta x_{\rm N}}^{n+1}, \tag{34}$$

  where $\widehat{u}_{\rm N} = \widehat{u}_{i,\rm face} {\rm N}_{i,\rm face}$ is the approximation for face-normal velocity and ${\rm N}_{i,\rm face}$ are the components of the face-normal. To compute the face-based pressure gradient, we make

Copyright © 2010 John Wiley & Sons, Ltd.

Prepared using fldauth.cls

use of the face and its two adjacent CVs (CV1 and CV2) as shown in figure 2c. The face-normal pressure gradient is discretized as:

$$\frac{\delta p}{\delta x_{\rm N}}^{n+1} = \frac{p_{\rm nbr}^{n+1} - p_{\rm cv}^{n+1}}{|\mathbf{S}_{\rm cv\rightarrow nbr}|}, \tag{35}$$

where the subscripts cv and nbr stand for the the control volume CV for which the velocity field is being solved and the neighboring CV sharing a common face, respectively and $|\mathbf{S}_{\rm cv\rightarrow nbr}|$ represents the magnitude of the vector connecting the two control volumes.

- **Step 5:** The pressure field and the pressure gradients at t^{n+1} are unknown in the above step. A pressure Poisson equation is derived by taking a discrete divergence of the above equations and solving for the pressure field at each control volume:

$$\sum_{\text{face of cv}} \Delta t \frac{\delta p}{\delta x_N}^{n+1} = \sum_{\text{faces of cv}} \rho_{\rm face}^{n+1} \widehat{u}_{i,\rm face} A_{\rm face} + V_{\rm cv} \frac{\rho_{\rm cv}^{n+3/2} - \rho_{\rm cv}^{n+1/2}}{\Delta t}. \tag{36}$$

- **Step 6:** Reconstruct the pressure gradient at the CV centers. The face-normal pressure gradient $\frac{\delta p}{\delta x_N}$ and the gradient in pressure at the CV-centroids are related by the area-weighted least-squares interpolation [40, 39]:

$$\epsilon_{cv} = \sum_{\text{faces of cv}} \left(P'_{i,\rm cv} \mathrm{N}_{i,\rm face} - P'_{\rm face} \right)^2 A_{\rm face}, \tag{37}$$

where $P'_{i,\rm cv} = \frac{\delta p}{\delta x_i}$ and $P'_{\rm face} = \frac{\delta p}{\delta x_{\rm N}}$.

- **Step 7:** Compute new face-based velocities, and update the CV-velocities:

$$u_{\rm N}^{n+1} = \widehat{u}_{\rm N} - \frac{\Delta t}{\rho_{\rm face}^{n+1}} \frac{\delta p}{\delta x_{\rm N}}^{n+1} \tag{38}$$

$$u_{i,\rm cv}^{n+1} = \widehat{u}_{i,\rm cv} - \frac{\Delta t}{\rho_{\rm cv}^{n+1}} \frac{\delta p}{\delta x_{i,\rm cv}}^{n+1} \tag{39}$$

5. NUMERICAL TEST CASES

The above numerical scheme is applied to different test cases in order to evaluate its accuracy. First, the accuracy of the numerical implementation are verified by conducting simple test cases with and without volumetric coupling. This includes potential flow field developed by an oscillating bubble, bubble dynamics due to imposed pressure variations testing the effectiveness of the adaptive time-stepping approach, and trajectory of a single bubble (with and without cavitation) in a vortical flow. Interactions of non-cavitating micro-bubbles with vortical flows are then investigated using the Euler-Lagrange volumetric coupling model and compared with other simulation techniques such as Euler-Euler two-fluid approach. Effect of large bubbles on a traveling vortex tube is used as a validation test case comparing the predictions of the volumetric coupling model with experimental data of Sridhar & Katz [55]. Also the capability of the bubble dynamics model together with large-eddy simulation in predicting small-scale cavitation and cavitation inception in a high-speed flow over an open cavity are tested by comparing with the experimental data of Liu & Katz [37]. Finally, LES of dense rising bubble plume in a liquid column is also conducted to study the effect of the volumetric coupling in capturing vortical flow field generated by the bubble motion. These numerical cases are described below.

Copyright © 2010 John Wiley & Sons, Ltd.

Prepared using fldauth.cls

5.1. Oscillating bubble:

A single air bubble is placed in water inside a cubical domain. A sinusoidal perturbation is imposed on the bubble. Bubble radius changes in time as $R_b = R_{b,0}(1-\epsilon \sin \omega t)$, where R_b and $R_{b,0}$ are the instantaneous and the initial radius, respectively, ϵ is the perturbation magnitude, ω is frequency and t is time. In this simulation, $R_{b,0} = 0.01 \times D$, where D is the cube size, and gives overall bubble concentration of 4×10^{-6}, $\epsilon = 0.1$, $\omega = 50$ [Hz]. One can derive the analytical expression for pressure, following the potential flow theory [45],

$$\frac{p(R) - p(\infty)}{\rho R_0^2 \omega^2} = -\epsilon \sin \omega t + \frac{2}{3}\epsilon^2 \left(1 - \frac{5}{2}\sin^2 \omega t\right), \tag{40}$$

where ρ is liquid density.

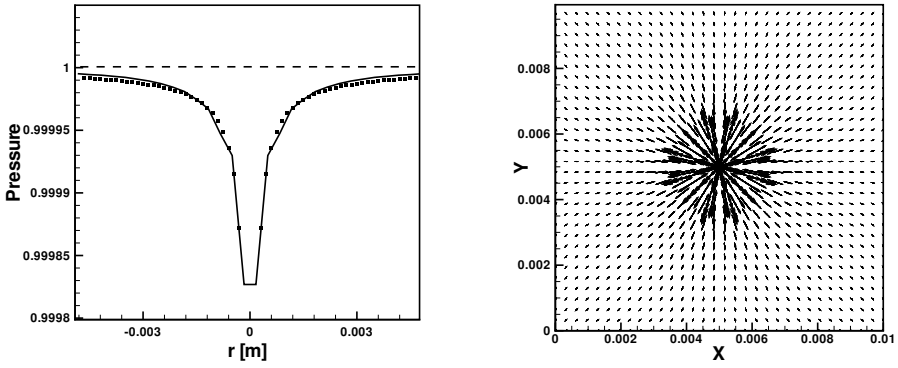

(a) Pressure Distribution (b) Velocity Vectors

Figure 4: Flow developed by an oscillating bubble: (a) Pressure distribution caused by volume displacement around the bubble (solid line) and two-way coupling alone (neglecting volume displacement effects, shown by dashed line) compared with analytical solution (symbols), (b) instantaneous velocity vector field due to bubble oscillations.

Figure 4a shows the radial distribution of hydrodynamic pressure around the bubble created by the size variation at $t^* = 0.3$ where $t^* = t/T$ and $T = 2\pi/\omega$. Also shown are the instantaneous velocity vectors due to bubble oscillation (Figure 4b). The pressure field is well predicted by the present numerical scheme with volumetric coupling effects whereas the two-way coupling alone does not predict any variations in pressure as shown by the dashed horizontal line. Note that the grid resolution used for this calculation is such that the bubbles are smaller or comparable in size to the control volume dimension. The domain size was considerably larger (10 times) than the bubble size (even at the maximum radius of the bubble). It was verified that he boundary effects were minimal in this test case by varying the domain size compared to the bubble size. The above result indicates that that the local variations in mixture density in momentum and continuity equation provide the correct solution even for a single, subgrid bubble with very low volume loading.

In another example two bubbles oscillating in tandem were considered [51]. Two similar bubbles were placed in a box and their radii change sinusoidally as above with a phase difference

Copyright © 2010 John Wiley & Sons, Ltd.

Prepared using fldauth.cls

of π [rad]. All properties were similar to the single bubble case, except they are both located $D/6$ away from the box center. The result is a doublet-like flow which is also well captured by the volumetric coupling model.

5.2. Bubble Dynamics Under Imposed Pressure Variations:

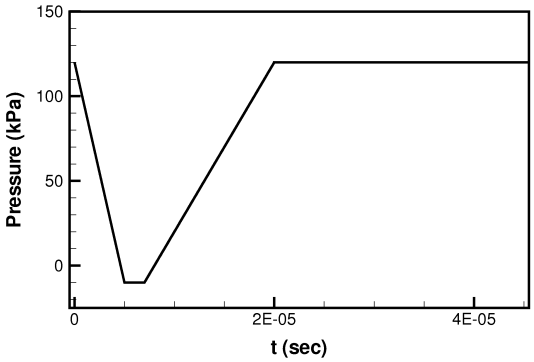

(a) Imposed outside pressure

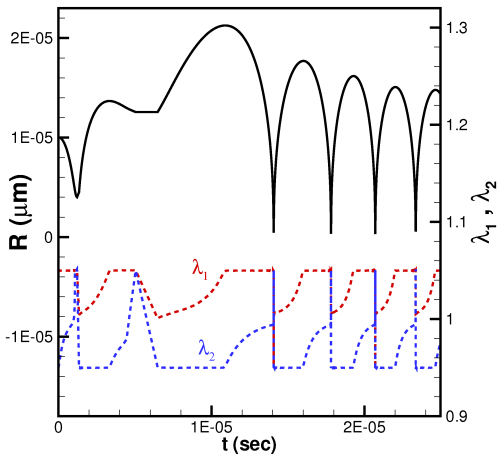

(b) $R(t)$, $\lambda_1(t)$, $\lambda_2(t)$

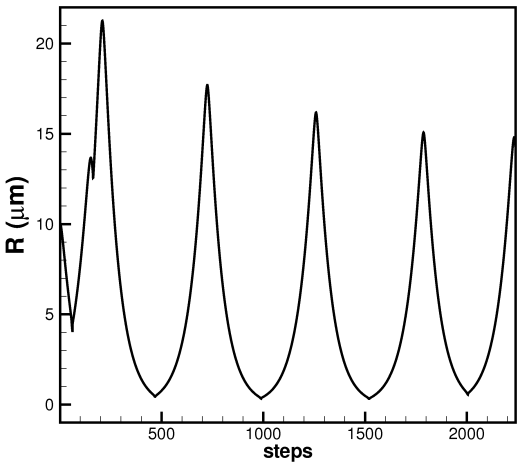

(c) Number of iterations

Figure 5: Time variation of bubble radius and eigenvalues ($\lambda_{1,2}$) for a cavitating bubble with imposed pressure variations.

To test the adaptive time-stepping approach, a numerical test case is considered wherein the external pressure is specified as a function of time and the bubble radius is computed using the Rayleigh-Plesset equation. This test case was also used by Alehossein & Qin [1] (denoted as AQ2007 henceforth) in their work on simulating cavitating bubbles in a convergent divergent nozzle. Figure 5a shows an imposed pressure variation to a stationary bubble. The fluid properties are those for water ($\rho_\ell = 1000\,\mathrm{kg/m^3}$, $\mu_\ell = 0.798\times10^{-3}\,\mathrm{kg/ms}$, $\sigma = 0.072\,\mathrm{N/m}$,

Copyright © 2010 John Wiley & Sons, Ltd.

Prepared using fldauth.cls

$p_v = 0.00424$ MPa). A bubble of initial radius ($R_{b,0} = 100$ μm, $dR_{b,0}/dt = 0$) is subjected to the outside pressure variation shown in figure 5a. The bubble undergoes growth and collapse as the outside pressure decreases and increases with time. Rapid accelerations and variations in bubble radius are observed. This test case is challenging for a numerical scheme based on constant time-steps. For an explicit Euler scheme, for example, a constant time-step on the order of 10^{-17} s would be required to capture the bubble growth and collapse and maintain a stable solution. Multiple periods of bubble oscillation would be very time-consuming for such an approach and adaptive time-stepping is essential. Figure 5b shows the solution obtained from the adaptive time-stepping. Also shown are the temporal variations in the eigenvalues λ_1 and λ_2 of the the coupled system of equations 24. Deviation of these eigenvalues from a value of unity correspond to rapid growth or decay period of the bubble and are good indicators for adaptive time-stepping. The time-step is thus changed if the eigenvalues depart from the unity value by 5% or more. With this approach stable solutions are obtained for much higher time-steps and multiple periods of bubble oscillation can be easily computed. Figure 5c shows that only around 2000 iterations are required to compute five periods of bubble oscillation. A time-step refinement study provided little variations in the predicted values of the bubble radius.

To analyze the robustness of the present stability theory-based adaptive time-stepping scheme, a similar test case as the above was considered. The outside pressure variation was similar to the above case, except that the range of pressure changes was from 12 kPa to -1 kPa, corresponding to the small pressure case by AQ2007 [1]. The initial bubble size is small (2 micron), chosen mainly because small bubbles exhibit strong sensitivity to outside pressure variation. Figure 6 compares the time evolution of the bubble radius as predicted by the present adaptive time-stepping scheme, the approach by AQ2007, and constant time-step fourth-order Runge-Kutta schemes. It is observed that the adaptive time-stepping criterion of the present approach is very robust providing stable and accurate evolution of the bubble radius.

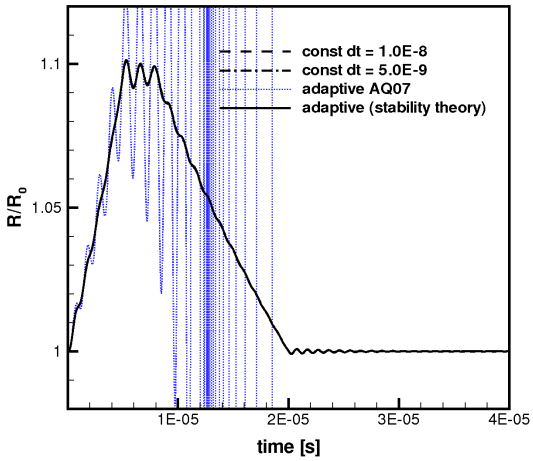

Figure 6: Comparison of the present stability theory based adaptive time-stepping approach with that of AQ2007 [1] showing robustness of the present criterion.

Copyright © 2010 John Wiley & Sons, Ltd.

Prepared using fldauth.cls

Table I: Computational parameters for the Rankine vortex.

Γ (m^2/sec)	V_∞(m/sec)	C_0(m)	a_c(m)	Re_{C_0}	ρ_ℓ(kg/m^3)
1.91511	12.5	0.6096	0.009486	7.62×10^6	1000
Grid Size	small	medium	large		
$N_{xy} \times N_z$	$118^2 \times 3$	$236^2 \times 4$	$472^2 \times 8$		

The robustness of the adaptive time-stepping was further tested in large-eddy simulation of small-scale cavitation in flow over an open cavity; wherein bubbles of different size are injected in the shear layer and undergo rapid variations in their radius due to spatio-temporal changes in the pressure field. This test case is presented later in section 5.5.

5.3. Bubble Trajectory in a Vortex:

Accurate prediction of bubble motion in a vortex is highly important since forces other than drag (i.e. lift and added mass) may become significant in this complex flow. We chose a line vortex configuration to evaluate the ability of the method to accurately compute the bubble trajectory in a vortical flow. A line vortex (often called Rankine Vortex) is a model for vortical flow generated at the tip of ship propeller blades [23]. The model consists of a forced vortex region in the core of the vortex, and a free vortex region outside the core. Flow velocity and pressure are defined as

$$u_\theta(r) = \left\{ \frac{\Gamma}{2\pi a_c^2} r \, , r \leq a_c; \quad \frac{\Gamma}{2\pi r} \, , r > a_c \right\} \tag{41}$$

$$p_\omega(r) = \left\{ p_\infty - \frac{\rho\Gamma^2}{4\pi^2 a_c^2} + \frac{\rho\Gamma^2 r^2}{8\pi^2 a_c^4}, r \leq a_c; \quad p_\infty - \frac{\rho\Gamma^2}{8\pi^2 r^2}, , r > a_c \right\}, \tag{42}$$

where u_θ is the angular component of velocity vector, $\Gamma = \pi a_c^2 \omega$ is the vortex circulation, ω is vorticity inside the core, r is the radial distance to the vortex center, and a_c is the vortex core radius, within which the circulation is constant, and outside of the core is zero. Vortex core size, vorticity, and circulation which are functions of the velocity in z direction (V_∞) and chord length of the propeller (C_0).

Motion of a single air bubble in a line vortex is simulated using the discrete bubble model with volumetric coupling. This test case shows the ability of the method to accurately predict the bubble motion in a relatively complex flow on an unstructured grid. The flow configuration is the same as medium scale vortex used by [23] and listed in the table I. Bubble diameter and density are $d_b = 100$ μm and $\rho_b = 1$ kg/m^3, respectively and it is initially located at $r = 9$ mm from the vortex center.

A cylindrical domain is chosen for this test case. Boundary conditions are wall on the peripheral boundary and periodical on the xy-plane. The computational grid is shown in figure 7. A grid convergence study is conducted by performing simulations at three different resolutions as shown in Table I. The numerical simulation results are compared to the Rankine vortex model to calculate the error associated with the single phase flow itself. Figure 8 shows *L2* norm for error in the horizontal velocity component indicating a second-order accuracy. The error is defined as $u_{error} = |(u_{comp.} - u_{model})|/u_{max}$, where $u_{comp.}$ and u_{model} are velocity of a particular location from computation and Rankine model, respectively, and u_{max} is maximum velocity in the domain.

Copyright © 2010 John Wiley & Sons, Ltd.

Prepared using fldauth.cls

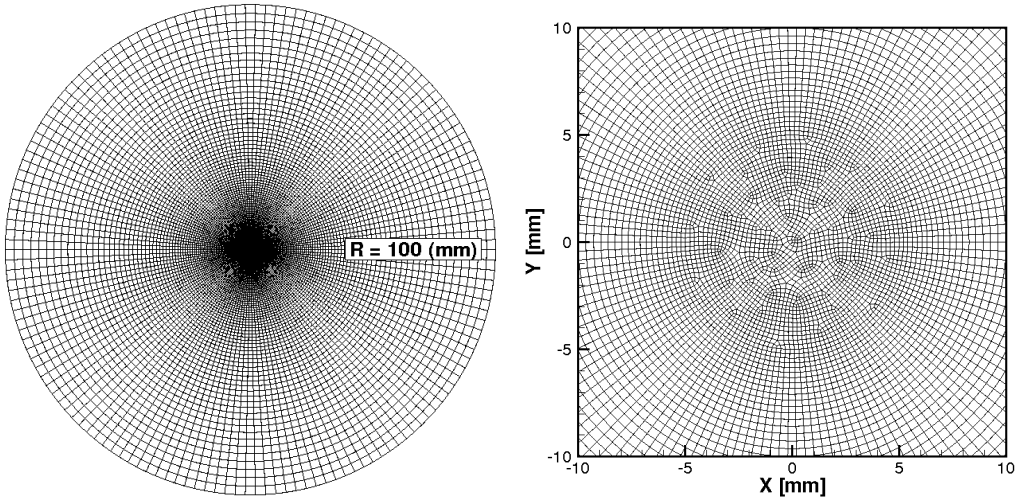

(a) entire domain in vortex plane (b) grid refinement in the vortex core

Figure 7: Computational grid for the Rankine vortex simulations (coarse grid is shown.)

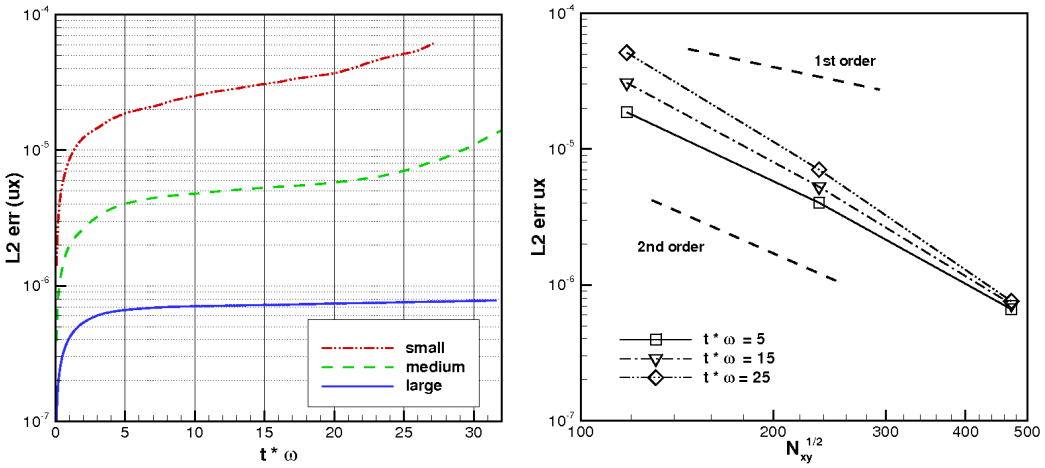

(a) error versus time (b) error versus grid size

Figure 8: Time evolution of L2 error in the horizontal velocity component for the Rankine vortex.

Copyright © 2010 John Wiley & Sons, Ltd.

Prepared using fldauth.cls

5.3.1. Non-Cavitating Bubble: Trajectory of a single bubble with 100 μm diameter and density of 1 kg/m^3 is studied in the Rankine vortex. Bubble is initially located close to the vortex edge at $r_0/a_c = 0.95$. The initial velocity is set to the local flow velocity, which is almost the maximum velocity in the domain. Different force models include drag, lift, added mass, pressure, and buoyancy force. Figure 9 shows the trajectory of the bubble indicating a spiral trajectory towards the vortex center, mainly under influence of drag, added mass, and pressure force. The figure compares the trajectory obtained using two approaches for different grid resolutions: (i) the fluid velocity and pressure fields used in the computation of the forces on the bubble (for example, drag, lift, added mass, pressure force etc.) are obtained from the solution of the Navier-Stokes equations, (ii) the fluid and pressure fields are taken from the exact solution of the Rankine vortex (equations 41) at the bubble location.

The first approach includes the interpolation errors from the grid control volume to the bubble location, time and space integration of the fluid flow and the discrete bubble equations. The latter approach basically provides the true trajectory of the bubble if the effect of the bubble motion on the fluid flow is neglected. For a large section of the bubble trajectory, all three grid resolutions show very close agreement with the direct integration result. Near the vortex center; however, the coarse grid is less accurate, due to insufficient grid resolution (shown in figure 9(b)).

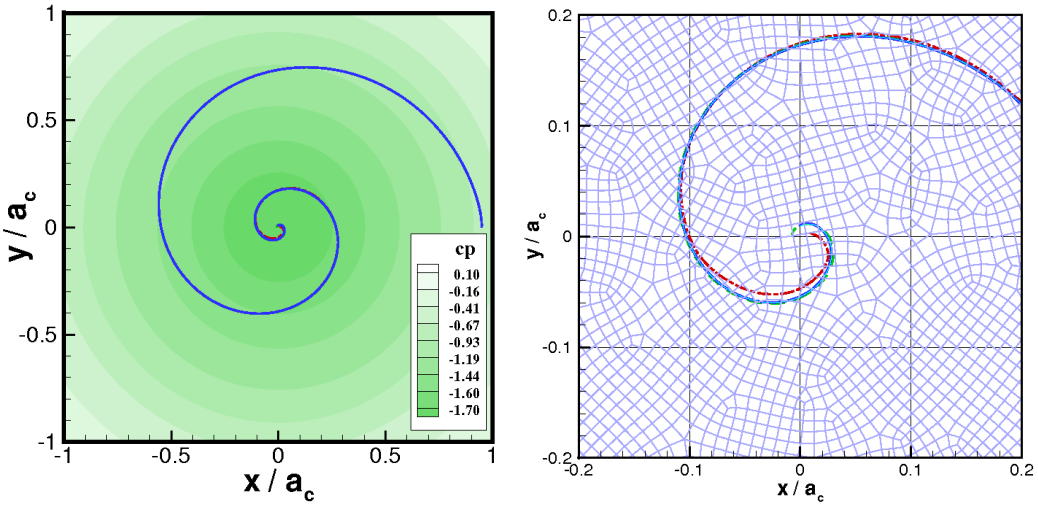

(a) *BubbletrajectoryandC_p* contours (b) medium grid shown

Figure 9: Trajectory of single bubble using small (dash-dotted red line), medium (dashed green line), and large (solid blue line), in comparison to the results from direct integration of equations of motion in Rankine vortex model (solid cyan line).

In order to further quantify the accuracy of the bubble trajectory, an L2 error in trajectory is monitored (figure 10). Here the error is defined as $r_{err} = |(r_{comp} - r_{dirint})|/a_c$, where r_{comp}, and r_{dirint} are bubble distance to the vortex center from the computation and direct integration, and a_c is the vortex core radius. The error is integrated in time to calculate the L2 norm. Close to second order convergence is observed.

Copyright © 2010 John Wiley & Sons, Ltd.

Prepared using fldauth.cls

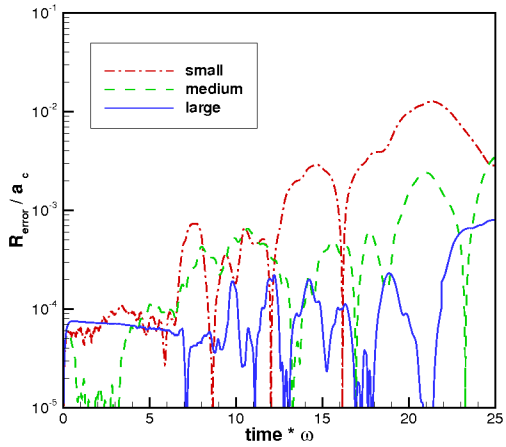

(a) error of radius calculation with different number of grids

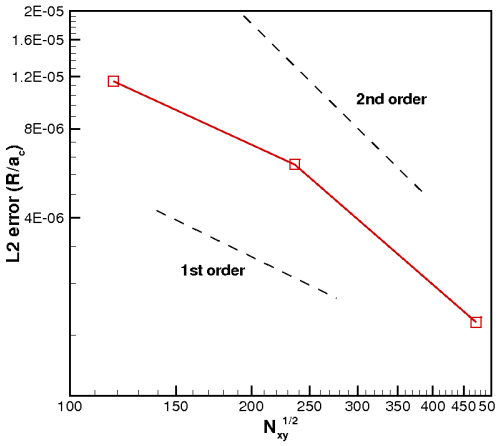

(b) L2 error for different number of grids

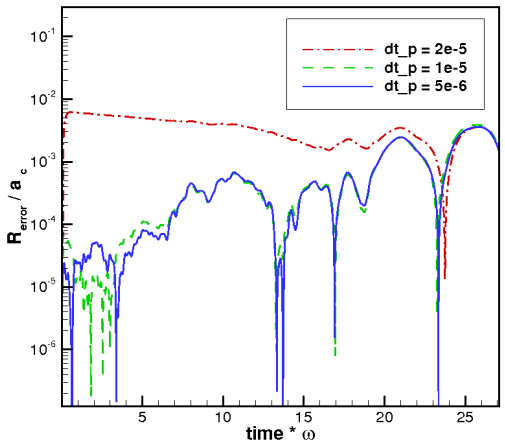

(c) error of radius calculation with different time steps

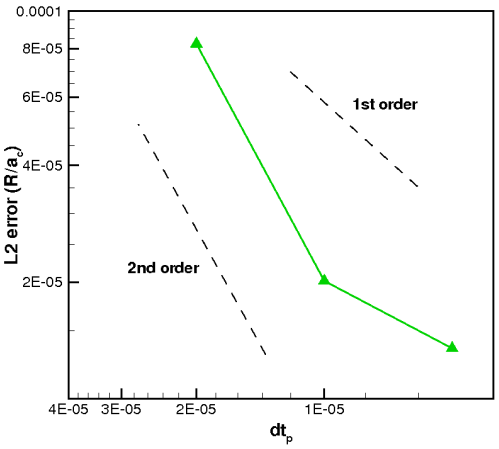

(d) L2 error for different time steps

Figure 10: Error in the trajectory of a single non-cavitating bubble in a Rankine vortex,

5.3.2. Cavitating Bubble: In this test case, we compare trajectories of a single bubble in Rankine vortex, with and without cavitation. When the bubble travels to the vortex center, it starts growing due to the decreasing pressure towards the vortex center. It is important to have a smooth representation of the pressure field seen by the bubble (P_∞) as the bubble goes from one control volume to another. The pressure seen by the bubble is basically obtained by interpolating the pressure gradient from the $faces$ of the cv to the cv centers using the least-squares interpolation consistent with the pressure reconstruction. The pressure field at any point within the cv centers is then obtained by using a linear interpolation in space as well as linear interpolation in time. This preserves the continuity of the pressure field from one cell

Copyright © 2010 John Wiley & Sons, Ltd.

Prepared using fldauth.cls

to another. In the present model, we do approximate that the outside pressure (or the pressure seen by the bubble) by interpolating it to the bubble center. Chahine and co-workers [23] have developed a Surface Average Pressure (SAP) model to more accurately represent the pressure field seen by the bubble. Knowing the size of the bubble and assuming a spherical bubble, this model can be easily implemented into the present framework as well (with little additional cost). However, for present test case this surface averaging of the pressure was not included.

Bubble growth changes the effect of the different forces on the bubble trajectory. Figure 11 shows trajectory of a 23 μm bubble with and without cavitation. The bubble moves towards the

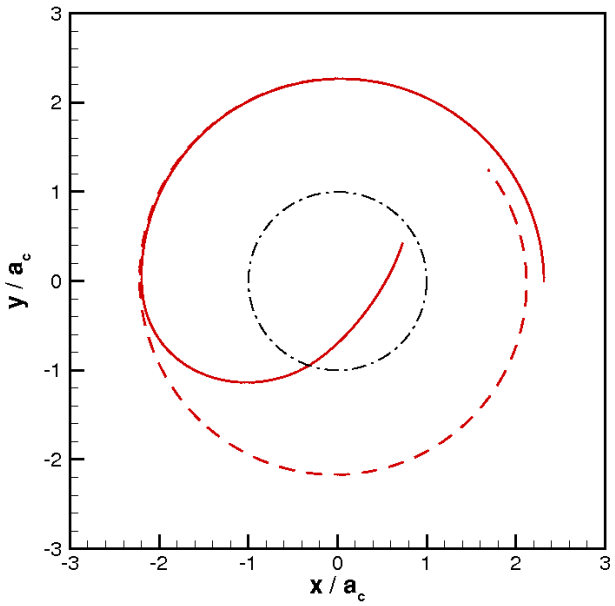

Figure 11: Trajectory of cavitating (solid line) versus non-cavitating (dashed line) bubbles in a Rankine vortex. The dash-dot line shows the vortex core.

center very slowly, since the flow acceleration is small at the initial radial location ($r_0 = 2.4a_c$). But once it faces a slightly lower pressure region at $r = 2a_c$, it starts growing. When the bubble grows the added mass effect and pressure force effect grow and it accelerates faster towards the center. Once the bubble enters the core, growth continues unrealistically (since there is no feedback effect on the flow in this test case to stop the growth) until gravity becomes important and it starts rising then.

5.4. Bubble-Vortex Interactions:

Interaction of multiple bubbles with vortical structures is important for many turbulent and separated flow structures. For example, turbulent cavitating flows involve highly separated flow structures behind propeller blades giving rise to tip vortices that can be modeled by a Rankine vortex [23], traveling vortex rings generated during propulsion and crashback [29], or recirculation regions over hydrofoil structures. In this section, we test the discrete bubble model's capability in accurately capturing the interaction of bubbles with vortical flows.

Copyright © 2010 John Wiley & Sons, Ltd.

Prepared using fldauth.cls

Specifically, we investigate: (i) large number of micro-bubbles in decaying Taylor-Green vortex, and (iii) a few large bubbles in a traveling vortex tube. The first case is based on the Euler-Euler two-fluid modeling of bubble-vortex interaction by Ferrante and Elghobashi [18] and allows comparison of the discrete bubble model with the two-fluid model. The second case is based on the experiments by Sridhar and Katz [54, 55] on bubbles entrained in a vortex ring and provides validation of the volumetric coupling effects.

5.4.1. Taylor-Green Vortex: Taylor-Green vortex is a two dimensional decaying vortex which has exact solution of Navier-Stokes equations for a single phase, incompressible flow. It is frequently reported as a test case for validation of numerical schemes for single phase flows. The flow velocity component is given as:

$$U_x = -\omega_0 \frac{k_y}{k^2} \exp(\nu k^2 t) \cos(k_x x) \sin(k_y y), \tag{43}$$

$$U_y = -\omega_0 \frac{k_x}{k^2} \exp(\nu k^2 t) \sin(k_x x) \cos(k_y y), \tag{44}$$

where ω_0 is the initial vorticity, k_x and k_y are wave number in x and y direction, $k^2 = k_x^2 + k_y^2$, and ν is the kinematic viscosity.

In a vortical flow, bubbles start migrating to the vortex center, essentially due to added mass and pressure gradient effects as shown by Ferrante and Elghobashi [18] (whose work will be referred to as FE07 henceforth). We choose one of the cases from FE07 (case a), to compare our Euler-Lagrange results to their Euler-Euler two-fluid computations. We use a tetrahedral unstructured mesh for these simulations. Bubbles start migrating in spiral routes towards the vortex centers (high enstrophy regions), mainly under the influence of the effects from pressure gradient and added mass (in this flow $\mathrm{D}\mathbf{u}/\mathrm{D}t$). Bubble concentration in the high enstrophy regions starts growing and consequently this motion modifies the flow field. Their results show that, micro bubbles with small initial volume fraction (~ 0.01) can remarkably modify the vortex.

Figure 12 shows the time variation of bubble concentration at the vortex center in comparison to the results of FE07. Both results from one-way coupling and volumetric coupling compare well with the Euler-Euler two-fluid computations from FE07. Figure 13 shows the modified flow vorticity in axial direction and in time. Our one way coupling result, match perfectly with the two-fluid formulation. The volumetric coupling effects also show similar trends. Small variations are mainly due to differences in the models. The variations in bubble concentrations in the initial times is close to the Euler-Euler simulation by FE07; however, at later times our predictions are slightly higher. This difference is perhaps due to the numerical diffusion present in the Euler-Euler scalar-transport models nature of the Euler-Euler models. In the present Euler-Lagrange scheme, however, the Lagrangian tracking is accurate to second-order accuracy as shown in earlier test cases.

5.4.2. Traveling Vortex Tube: Interactions of micro-bubbles with a traveling vortex corresponding to the experiments by Sridhar and Katz [54, 55] are investigated. Specifically, Sridhar & Katz observed that eight small bubbles, once entrained into a vortex ring, could deform the ring significantly. The simulations are setup to investigate if the discrete bubble model with volumetric effects can capture this phenomenon.

The computational domain and the evolution of an undisturbed pair of vortex tubes are shown in Figure 14. There is an inflow boundary at the left wall, an outflow condition at

Copyright © 2010 John Wiley & Sons, Ltd.

Prepared using fldauth.cls

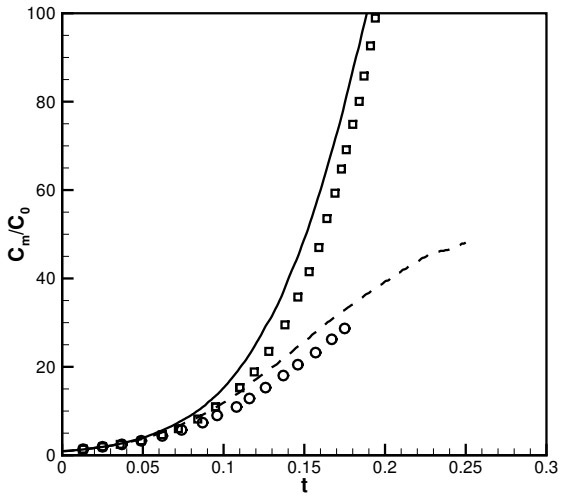

Figure 12: Bubble concentration (normalized by maximum initial value) at the vortex center from one-way coupling (solid line), and volumetric coupling (dashed line), in comparison to one-way (squares) and volumetric (circles) coupling simulation from FE07 [18].

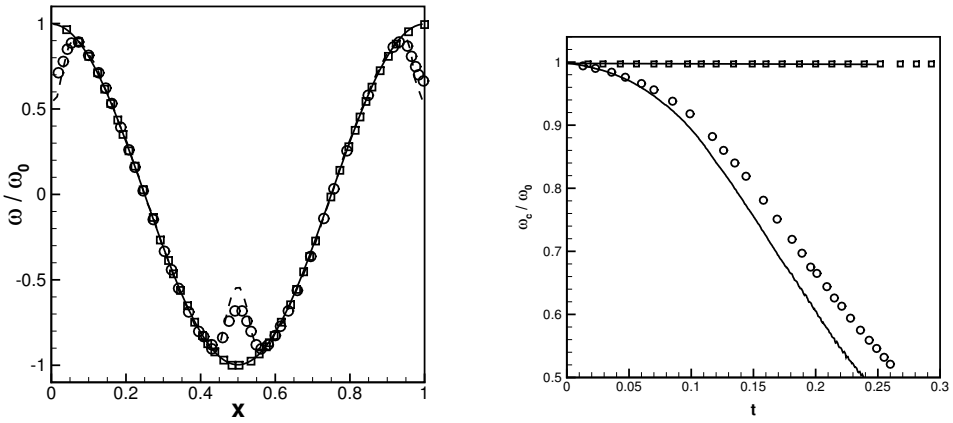

(a) Axial distribution of vorticity at $t = 0.2$ (b) Time variation of vorticity at the vortex center

Figure 13: Flow vorticity (normalized by maximum initial value) in comparison to the simulation by FE07.

Copyright © 2010 John Wiley & Sons, Ltd.

Prepared using fldauth.cls

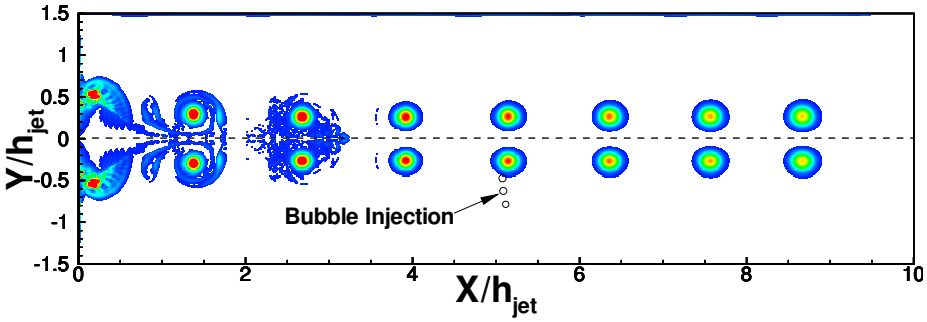

Figure 14: Computational domain and vortex tube evolution: (a) Two, symmetric vortex tubes are created by an inlet jet pulsed at $X = 0$. Contours show vorticity out of the plane as the undisturbed vortex travels downstream. Location of bubble injection is $X/h_{jet} = 5.0$

the right boundary, and walls on the top and bottom. The total domain size is $X/h_{jet} = 10$ by $Y/h_{jet} = 3$ and is centered at $Y/h_{jet} = 0$. At the left inlet boundary, a jet is pulsed for 0.27 seconds into the initially quiescent domain, which causes the roll up of two symmetric vortex tubes. The contours in figure 14 show the diffusion of high vorticity as the vortex tube travels downstream. Table II lists the computational parameters used in this study. The inflow velocity is a function of time, and is described by a sixth-order polynomial to match the experimental conditions. To keep the size of the computation small, a two-dimensional domain is simulated with periodic conditions in the spanwise direction giving rise to a vortex-tube. A uniform Cartesian grid is used throughout the area below the line of symmetry with a total of 800×121 elements in the X and Y directions.

Table II: Parameters for the traveling vortex tube case.

Parameter	Value
ρ_l, ν_l	$1,000\ kg/m^3$; $10^{-6}\ ms^{-2}$
Domain Size	1m $\times$ 0.15m $\times$ 0.005m;
Grid Size	$800 \times 121 \times 4$
Jet height (h_{jet})	0.1 m
Inflow Time	0.27 s
Initial Vortex Strength, $\Gamma_0(m^2s^{-1})$	0.0159, 0.0207, 0.0254
Bubble Size (μm)	500, 700, 900, 1,100
Inflow Velocity	$U(t) = \sum_{n=0}^{6} a_n t^n$
a_6, a_5, a_4, a_3	62278; -47082; 13686; -2062
a_2, a_1, a_0	159.5; -1.289; 0.006

At a value of $X/h_{jet} = 5.0$, eight bubbles are injected below and in front of the vortex core. Due to buoyancy, the bubbles rise around the rear of the vortex and are swept into the downward velocity region on the forward side of the passing core. A parametric study is performed to determine how bubble settling location and vortex structure are affected by bubble size and vortex strength. Depending on the Stokes number, the bubbles may circle

Copyright © 2010 John Wiley & Sons, Ltd.

Prepared using fldauth.cls

the core multiple times before ultimately reaching their final settling location, where their average motion relative to the vortex center is zero. Once they have reached this state, the settling coordinates (r_s, θ_s) are averaged over all bubbles and in space over a distance of $5.2X/h_{jet} < X_{vx} < 5.8X/h_{jet}$. The average settling radius for each case is plotted against the non-dimensional parameter $\mathbf{g}d_b^3/8\Gamma_0^2$ (ratio of buoyancy force to hydrodynamic pressure gradient) in figure 15 alongside the experimental data. Even at this small overall volume fraction, the local volume displacement effects are crucial in obtaining the correct bubble settling radius, particularly as the ratio of bubble size to vortex strength is increased. In obtaining these results, the lift coefficient measured by Sridhar & Katz [54] was used; $C_L = 0.22\alpha^{-3/4}$, where α is the local shear rate.

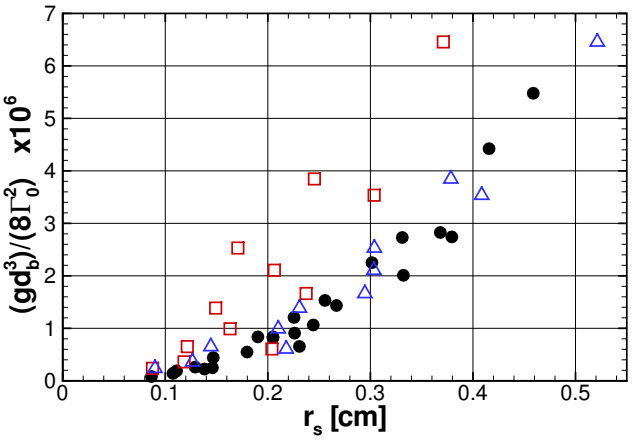

Figure 15: Comparison of the non-dimensional settling location with the experimental results of Sridhar & Katz [55]. The parameter $\mathbf{g}d_b^3/8\Gamma^2$ is the non-dimensional ratio of the buoyancy force and the hydrodynamic pressure gradient experienced by the bubble. (●) Experimental data, □ simulations with two-way coupling (neglecting volumetric effects), △ simulations with the volumetric displacement effects.

Importantly, significant vortex distortion is predicted by the numerical model for certain bubbles with parameters similar to those observed in the experiments. In the absence of the bubbles, the vortex core is stable. In the presence of some entrained bubbles, the vortex core deforms, altering the vorticity distribution as shown in figure 16. The contours of vorticity in figure 16a are shown approximately 1 second after bubble entrainment. The core has been fragmented into several regions of higher vorticity. The average radial vorticity distribution (figure 16b) shows that the volumetric displacement of the fluid due to bubble motion has resulted in a decrease of inner core vorticity, while a band of high vorticity has been created just outside of the bubble settling radius. The vortex distortion was found to be predominantly an effect of variations in the void fraction as the bubbles travel to their settling location. This was confirmed by computing the bubble trajectories without considering the void fraction variations. With two-way coupling and neglecting volumetric displacement effects (i.e. Θ_ℓ set equal to 1), vortex distortion was not obtained for any of the cases studied. This test case confirms the effectiveness of the present numerical model in properly predicted bubble-vortex interactions.

Copyright © 2010 John Wiley & Sons, Ltd.

Prepared using fldauth.cls

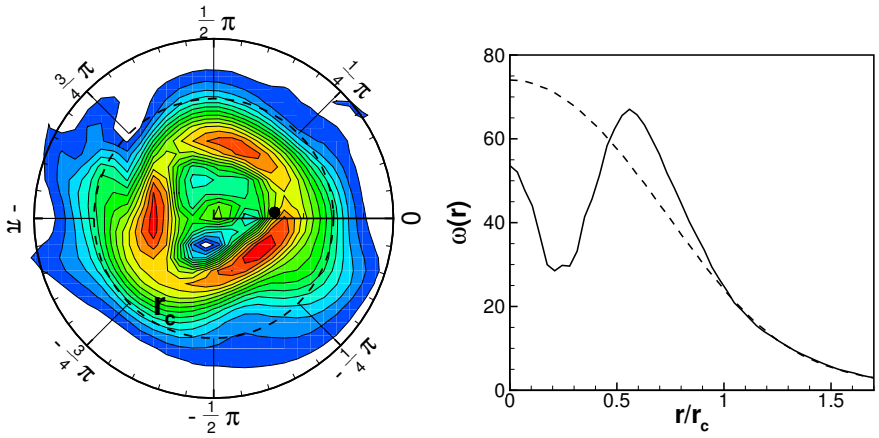

(a) Vorticity contours (b) Radial vorticity distribution

Figure 16: Vortex distortion by the entrained bubbles ($d_b = 1,100\mu m$ bubbles; $\Gamma_0 = 0.0159\ m^2 s^{-1}$) : (a) vorticity contours and average bubble location (black dot), (b) radial mapping of vorticity. (—) with void fraction variations, (- -) without accounting void fraction variations.

It should be noted that the intention of this test case was to indicate the effectiveness of volume displacement effects in predicting the vortex distortion phenomenon. However, the experiments are three-dimensional, whereas we use a two-dimensional approximation in present work in order to be able to perform several parametric studies. For this reason, the level of vortex distortion observed in the experiments cannot be compared directly to that predicted by the simulations. However, the qualitative trend as predicted by the volumetric effects is compared with the experimental data as opposed to purely two-way coupling effects.

5.5. LES of Small Scale Cavitation and Inception in Flow Over an Open Cavity:

This flow configuration is based on the experimental study of Liu and Katz [37] (will be referred to as LK2008 henceforth); wherein high-speed flow over a nearly square cavity is studied. The Reynolds number based on the cavity length (see figure 17) 170,000 and upcoming stream to the cavity section is fully turbulent, due to the presence of tripped section at the inlet ramp to the cavity (see [37] for the details). They have shown that cavitation occurs near the trailing edge of the cavity and on the shear layer (for low cavitation indices). Upstream flow velocity is 5 m/s, cavity length (L) and (D) are 38.1 and 30 mm, respectively. We performed a large eddy simulation of this flow to study small-scale cavitation and cavitation inception using the discrete bubble model. In our study, bubbles of different sizes are injected upstream of the cavity and their size variation due to the pressure fluctuation on the shear layer is modeled by solving Rayleigh-Plesset equation. Outside pressure variations are directly taken from the pressure data at the bubble location.

The computation is performed on a grid (figure 17) with predominantly orthogonal, hexahedral elements together with unstructured grid connectivity. Three different

Copyright © 2010 John Wiley & Sons, Ltd.

Prepared using fldauth.cls

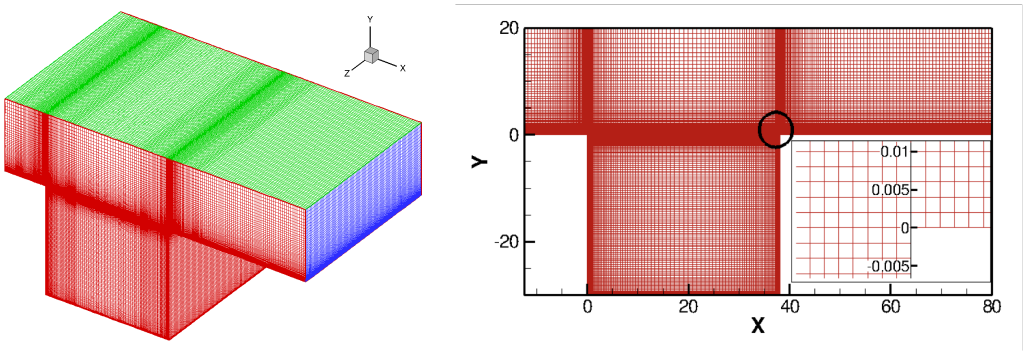

(a) 3D View (b) Symmetry Plane

Figure 17: Computational domain and grid: (a) three-dimensional domain with Cartesian grid, (b) refined grids (dimensions shown are in mm) are used in the shear layer and near the cavity leading and trailing edges. A zoomed-in view of the grid near the trailing edge is shown in wall co-ordinates.

computational grids are used to study grid dependency. The total number of elements is nearly 5 million with approximately 2 million grid elements inside the shear layer. The smallest grid size is 1.1 in wall units. More details of the simulation settings are shown in Tables III and IV.

Table III: Properties for flow over cavity (+ denotes wall units, $y^+ = yu_\tau/\nu$).

Average inflow velocity	$\overline{U_\infty} = 5.175$ m/s
Kinematic viscosity	1.121×10^{-6} m^2/s
Reynolds number	$Re_L = 170,000$
Vapor pressure	$P_v = 2.337$ kPa

Table IV: Cavity geometry and computational grid (+ denotes wall units, $y^+ = yu_\tau/\nu$. $u_\tau \approx 0.42$ at a point upstream of the leading edge). Base grid is refined in all directions compared to coarse grid. Fine grid is refined in spanwise direction compared to base grid.

Geometry and parameters	Cavity size	$38.1 \times 30 \times 50.8$	mm^3
	Duct size	$92.4 \times 20 \times 50.8$	mm^3
	Cavity length L	38.1 mm	
	Average inflow velocity, U_∞	5 m/s	
	Reynolds number $Re_L = \frac{U_\infty L}{\nu}$	170,000	
coarse grid	$\Delta x_{min} = \Delta y_{min}$, $\Delta x^+_{min} = \Delta y^+_{min}$	3.8 μm, 1.3	
(6×10^5)	Δz, Δz^+	1000 μm, 348	
base grid	$\Delta x_{min} = \Delta y_{min}$, $\Delta x^+_{min} = \Delta y^+_{min}$	1.9 μm, 0.67	
(5×10^6)	Δz, Δz^+	500 μm, 174	
fine grid	Δy_{min}, Δy^+_{min}	2.0 μm, 0.7	
(7×10^6)	Δz, Δz^+	200 μm, 69	

Copyright © 2010 John Wiley & Sons, Ltd.

Prepared using fldauth.cls

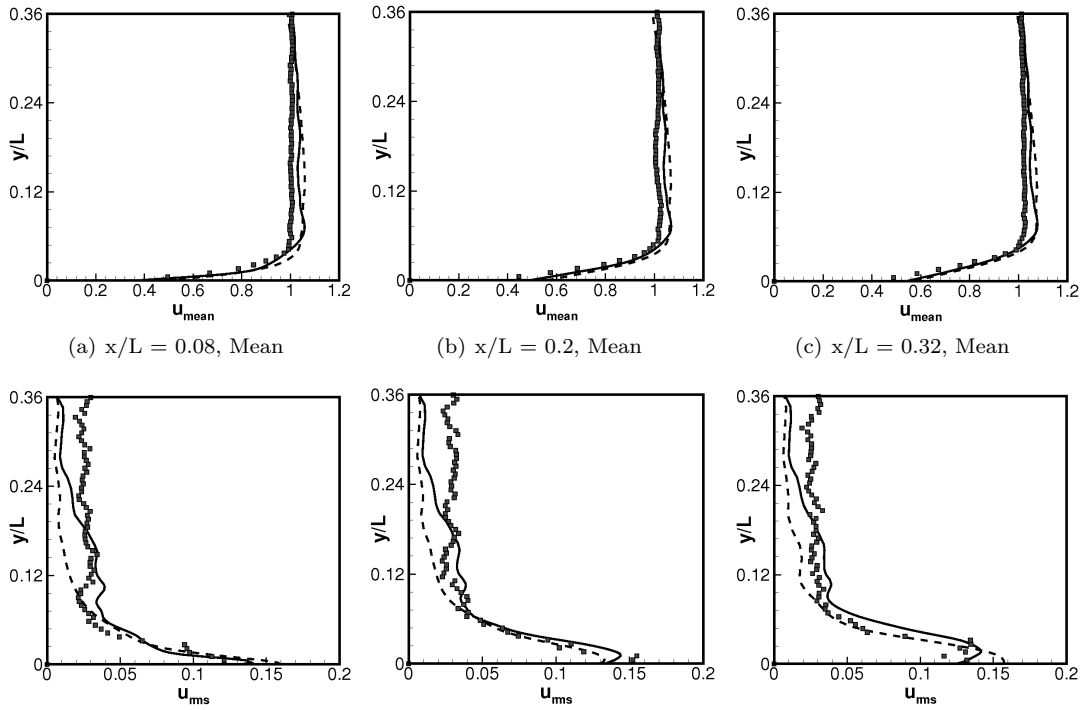

(a) x/L = 0.08, Mean (b) x/L = 0.2, Mean (c) x/L = 0.32, Mean

(d) x/L = 0.08, RMS (e) x/L = 0.2, RMS (f) x/L = 0.32, RMS

Figure 18: Effect of grid refinement on the mean and *rms* of stream-wise flow velocity component. Shown in the figures are the results from the fine (solid line), coarse (dashed line) computational grid, and experimental data (symbols) of LK2008.

In the present simulation, the turbulent boundary layers are resolved, and no-slip conditions are applied at all walls. A convective outflow boundary condition is applied at the outlet. In the experimental setup, the upstream region of the duct consists of a convergent section near the bottom wall and the flow is tripped using thirteen notches to create turbulence [37]. In the experiments, there was also a significant amount of vertical velocity in the downward direction, possibly obtained because of the convergent section in the upstream part of the duct. The divergent section is not simulated in the present study. Instead, it is assumed that the flow is fully developed and the experimentally measured mean velocity field in the symmetry plane is used to specify the inlet conditions. To create proper turbulence structures, a separate periodic flow in a duct is simulated at the desired mass-flow rate and Reynolds number using a body-force technique [46]. The Reynolds number based on the friction velocity for the inflow duct is very high ($Re_\tau = 7500$). To match the mean flow with the experimental data, we use the mean flow field from the experiments and the instantaneous velocity fluctuations from the periodic duct flow as inlet conditions for the cavity calculation. In order to show the accuracy of the flow simulation, a comparison of the flow velocity statistics to those of experiment is presented.

Figure 18 shows the mean and rms of horizontal velocity distribution against experimental

Copyright © 2010 John Wiley & Sons, Ltd.

Prepared using fldauth.cls

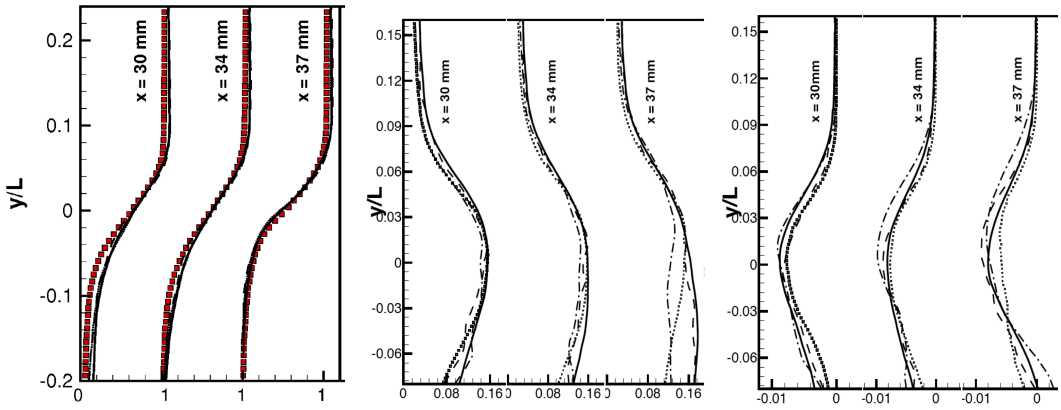

(a) Mean Velocity (b) RMS Velocity (c) Reynolds Stress

Figure 19: Comparison of velocity statistics in the vertical direction near the trailing edge: (a) $\frac{\overline{u}}{U_\infty}$, (b) $\frac{u_{rms}}{U_\infty}$, (c) $\frac{\overline{u}v}{U_\infty}$, where $U_\infty = 5\ m/s$ is the upstream velocity. Symbols are experimental data (LK2008), lines correspond to present simulations fine (solid line), base (dotted line) coarse (dashed line).

results near the leading edge of the cavity for the fine and coarse grid resolutions. The mean flowfield is captured reasonably well by both grids. RMS values, however, show more substantial dependence on the grid resolution. Better agreement achieved with the finer grid, especially away from the boundary layer edge. Figure 19 shows comparison of normalized mean velocity, *rms* velocity and Reynolds stress near the trailing edge, again showing good comparison on fine grid. Owing to the large friction Reynolds number for upstream duct flow, precise predictions of the rms fluctuations compared with experimental data is difficult even for large-eddy simulation in the wall-bounded region. Detailed comparisons of the flow statistics over the shear layer and the trailing edge showed reasonable predictive capability of the present LES (for the mean and rms fluctuations) on fine grids [51]. In addition, near the trailing edge (where the shear layer impinges), there are no homogeneous directions to average the dynamic Smagorinsky constant used in the LES subgrid model. This may influence the turbulence levels and further investigation of the subgrid LES model is needed.

Cavitation inception is studied using the discrete bubble model with adaptive time-stepping. The gas content in the liquid was assumed to be small (initial gas void fraction was assumed to be 10^{-5}). It is important for the bubble nuclei to pass through the small pressure regions above the cavity ('window of opportunity' to get drawn into low pressure regions and cavitate) [25]. Accordingly, air nuclei were distributed evenly in a small band around the shear layer. The bubbles were initially injected over a small region in stream-wise direction and in a band of 10 mm in the mid section of flow span. In order to keep the number of bubbles constant in the domain, bubbles were continuously injected near the leading edge and removed farther away from the trailing edge. Bubbles are released near the leading edge and their size changes according to the outside pressure variation on the shear layer. The initial bubble size and the cavitation index (σ_i) were varied to numerically predict the inception index as well as to investigate the sensitivity to the model parameters. Table V shows the parameter setup in

Copyright © 2010 John Wiley & Sons, Ltd.

Prepared using fldauth.cls

these studies.

Table V: Case studies to analyze cavitation inception using the Discrete Bubble Model.

Case	Figure Symbol	d_{initial} (μm)	σ_i
C1	square	10	0.4
C2	triangle	50	0.4
C3	circle	100	0.4
C4	diamond	50	0.9
C5	circle (filled)	50	1.4
C6	square (filled)	50	0.1

Figure 20 shows temporal evolution of bubble locations inside the shear layer and above the trailing edge. The size of the scatter symbols is scaled with respect to the size of the bubble. Accordingly, large size bubbles are obtained near the trailing edge. The initial pressure inside the bubble was set based on an equilibrium radius corresponding to the radius of the nuclei and its location in the domain. Using the Rayleigh-Plesset equations (3), at equilibrium conditions, the pressure inside the bubble can be obtained as: $P_b = \overline{P}_{out} + 2S/R_b$ (S is the surface tension coefficient). The bubbles are then advected using the adaptive time-stepping described earlier. On an average, approximately $100,000$ bubble trajectories are tracked at each instant. This also tests the robustness of the adaptive time-stepping procedure outlined earlier. Figure 21 shows the trajectories and bubble outside pressure variation in time for two different bubbles. Bubble radius and time are non-dimensionalized by initial radius and cavity flow through time of cavity, respectively. Figure 21 shows sharp variation of bubble radius near the trailing edge, where the pressure suddenly drops in the separation zone. For lower cavitation index, bubble growth in the trailing edge can be much larger. The sharp variations in pressure, causes a huge bubble growth, especially when the cavitation index is low. This needs to be handled with a very small time step to capture the collapse and rebound process properly. The adaptive time stepping method handles this behavior very well, without adding significant computational overhead for bubble dynamics. For upstream cavitation number of $\sigma_i \leq 0.4$, small-scale cavitation was observed on the shear layer in the experiments. The discrete bubble model predicted cavitation on the shear for lower values of $\sigma_i \sim 0.2$. However, a scalar-transport based model [51] did predict occurrence of cavitation on the shear layer for $\sigma_i \leq 0.4$. This suggests that for the discrete bubble model, it is critical for the bubbles to have sufficient time to be trapped into the vortical structures observed in the shear layer.

In order to gain better understanding of how different parameters such as the initial bubble size and cavitation index σ_i affect the inception and the behavior of bubbles, three different initial bubble sizes (10, 50, and 100 μm) were considered with a constant cavitation index ($\sigma_i = 0.4$). In addition, four different cavitation indices (0.1, 0.4, 0.9, and 1.4) were examined on a certain initial bubble diameter ($d_{init} = 50$ μm). Table V shows different diameters and cavitation indices used in the present study. Effect of cavitation index on the bubble cavitation is studied in more detail by performing PDF analysis on the bubble size distribution. This analysis is done on the entire bubbles in the whole simulation domain and also in three different zones of interests. These zones are defined on the shear layer (zone 1 and 2) and trailing edge

Copyright © 2010 John Wiley & Sons, Ltd.

Prepared using fldauth.cls

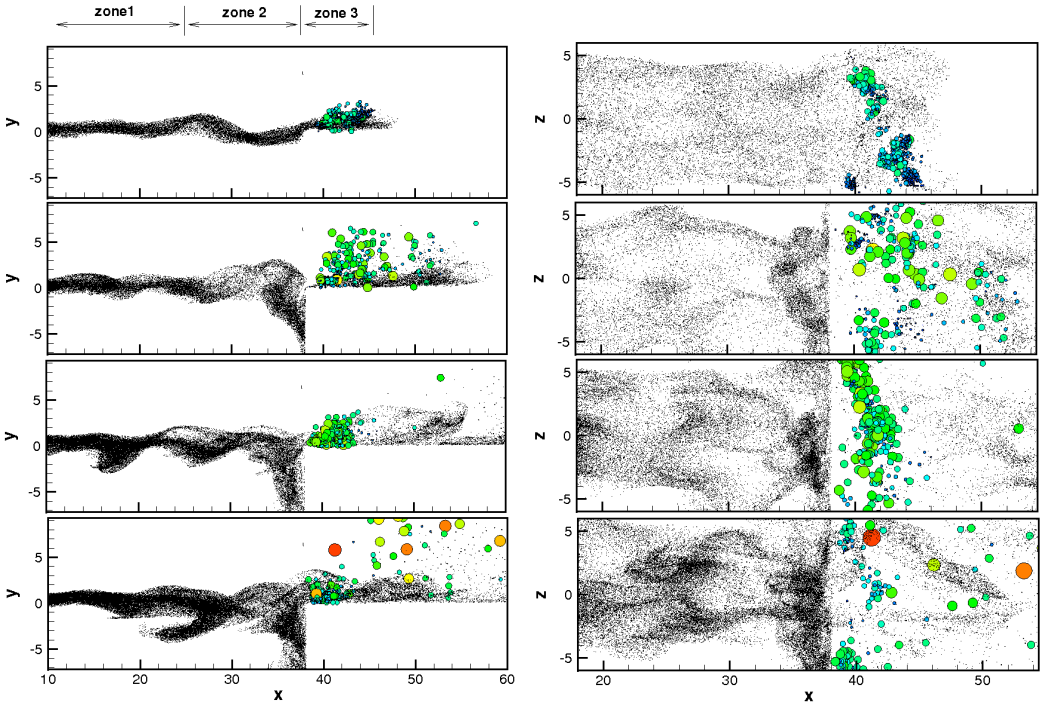

(a) side view (b) top view

Figure 20: Temporal evolution of bubble distribution (initial size 50 μm) on the shear layer for $\sigma_i = 0.4$: (a) side view showing entire shear layer and trailing edge, (b) top view above the trailing edge.

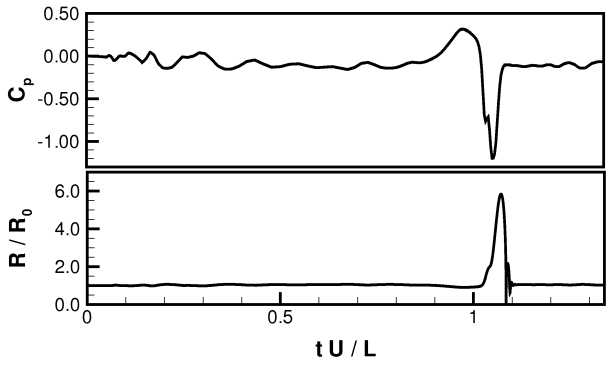

Figure 21: Temporal evolution of bubble radius (normalized by initial radius) and outside pressure coefficient (C_p) seen by the bubbles for two sample trajectories of bubbles released near the leading edge. The upstream pressure level is set based on $\sigma_i = 0.8$. Bubble is released at y = 0.2 mm from the leading edge surface.

Copyright © 2010 John Wiley & Sons, Ltd.

Prepared using fldauth.cls

(zone 3) and shown in figure 20. This analysis will clearly show which zones are more prone to cavitation and the effect of σ_i on the number of bubbles undergoing changes in diameter. Figure 22 shows the results of PDF analysis on the entire bubbles and also different zones.

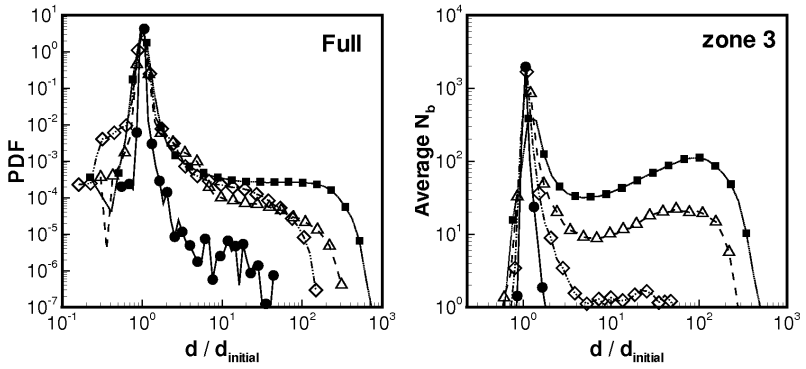

(a) (b)

Figure 22: Effect of cavitation index σ_i on the PDFs and average number of bubbles (N_b) sampled based on the growth ratio (d/d_{initial}) for case C2 (triangle symbols), C4 (diamond symbols), C5 (filled circles), and C6 (filled square): (a) PDF of all bubbles over the region of interest; (b) average number of bubbles in zone 3 (trailing edge).

Figure 22(a) shows that the majority of bubbles have not grown and they retain their initial size. This shows the importance of regional sampling in this analysis, since only a few bubbles have the chance of being trapped in the low pressure zone on the trailing edge. This figure shows that decreasing cavitation index σ increases the PDF of higher growth ratios for bubbles. PDF of growth increases up to three orders of magnitude for instance for bubbles of 10 times larger ($d/d_{init} = 10$). The maximum growth rate almost increases two orders of magnitude by decreasing σ from 1.4 to 0.1. Near the trailing edge, large differences in the average number of bubbles with the same growth ratio are observed (figure 22(b)). For the lowest σ_i (C6), number of large bubbles observed near the trailing edge is at least an order of magnitude more than other cases (C2, C4, and C5). The highest cavitation index nearly shows no cavitation above trailing edge. Numerically the inception index of 0.9 was predicted to be close to that observed in the experiments.

5.6. LES of Rising Bubble Column:

In this study, we demonstrate the effectiveness of our approach in simulating buoyancy driven dense bubbly flows. The geometry selected corresponds to the 'Becker case' [6], which has become an almost standard test case in the chemical engineering literature [52] [14] [13] [26]. The domain is shown in figure 23(a), and its characteristic dimensions are summarized in table VI. All boundaries are assigned a no-slip condition except for the top wall at $Y = 1.5$, where a slip condition ($u_y = 0$) is applied to approximate the experimental free surface. Air bubbles are continuously injected into the water filled domain from a disk located on the bottom wall with a flow rate of 1.6 l/min and a superficial gas velocity of $0.66m/s$. The injection disk is $0.04m$ in diameter and located $0.15m$ from the left hand wall. At this gas

Copyright © 2010 John Wiley & Sons, Ltd.

Prepared using fldauth.cls

flow rate, the fluid and bubble motion is known experimentally to be periodic in nature. We use this test case to see if the present methods can capture the transient behavior. We use a Dynamic Smagorinsky model to compute the subgrid scale fluid stress. In computing bubble motion, we use the lift and drag coefficients suggested by Darmana et al. [11] for a similar flow:

$$C_D = max\left[min\left[\frac{16}{Re_p}(1+0.15Re_p^{0.687}), \frac{48}{Re_p}\right], \frac{8}{3}\frac{Eo}{Eo+4}\right] \quad (45)$$

$$C_L = 0.5 \quad (46)$$

Table VI: Computational parameters used for the 2D bubble column case

L_x, L_x, L_x	0.5m, 1.5m, 0.08m
n_x, n_y, n_z	80, 150, 15
Gas Flow Rate	$1.6\ l/min$
Superficial gas velocity	$0.66mm/s$
Injection location	$(x, y, z) = (0.15, 0, 0)$
Injection area	$\emptyset_{inj} = 0.04m$
Bubble Diameter	$1.6mm$
Bubble Density	$1.2kg/m^3$
Liquid Density	$1,000kg/m^3$
Liquid Viscosity	$10^{-3}Ns/m^2$
Probe 'A' location	$(x, y, z) = 0.035m, 0.9m, 0.04m$
Probe 'B' location	$(x, y, z) = 0.45m, 1.05m, 0.04m$

In figure 23(b) we show the streamlines corresponding to the average velocity field in the X-Y midplane. In the lower half of the domain, a large clockwise vortex is generated by the bubbles rising along the left hand wall. The upper half is highly transient, and marked by the periodic migration of the bubble plume in the X direction. This migration corresponds with the growth and collapse of several secondary vortices in the upper regions of the domain. The periodicity of the bubble plume is shown in figure 24 where we have plotted 8 snapshots of instantaneous bubble positions, each 7 seconds apart. In figure 24a, the plume is firmly directed against the left wall through most of its length due to the strong lower vortex. A secondary, counter-clockwise vortex located in the upper left corner of the domain pushes the top of the plume to the right. In figures 24b through 24e, this secondary vortex strengthens and slides downward along the left hand wall, creating a bulge in the plume. This bulge cannot travel into the lower part of the plume due to the size and strength of the main circulation region, and eventually it collapses, as a new counter-clockwise vortex is created in the upper left corner (see figures 24f through 24h).

The periodic nature of the liquid phase is shown in figure 25, where we plot the vertical velocity in time for points 'A' and 'B' as shown in figure 23(a). The magnitude of the velocity peaks at these two points is similar to the values measured in the experiments of Sokolichin & Eigenberger [52]. We observe an average oscillation period of about 49 seconds, which is 8

Copyright © 2010 John Wiley & Sons, Ltd.

Prepared using fldauth.cls

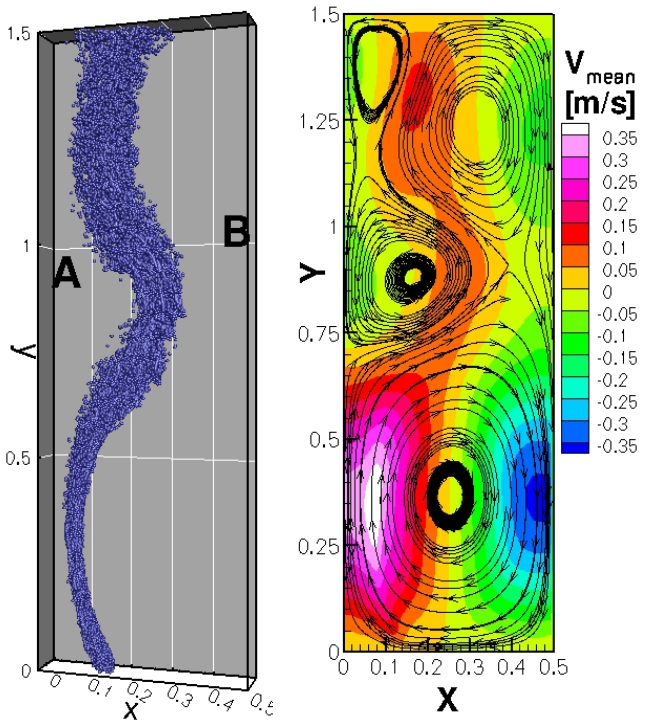

(a) Geometry (b) Avg. Velocity field

Figure 23: (a)Bubble column geometry showing the instantaneous bubble locations. Points A and B correspond to the location of two velocity probes. (b) Contours of time averaged Y component of fluid velocity. Streamtraces show the time averaged velocity field.

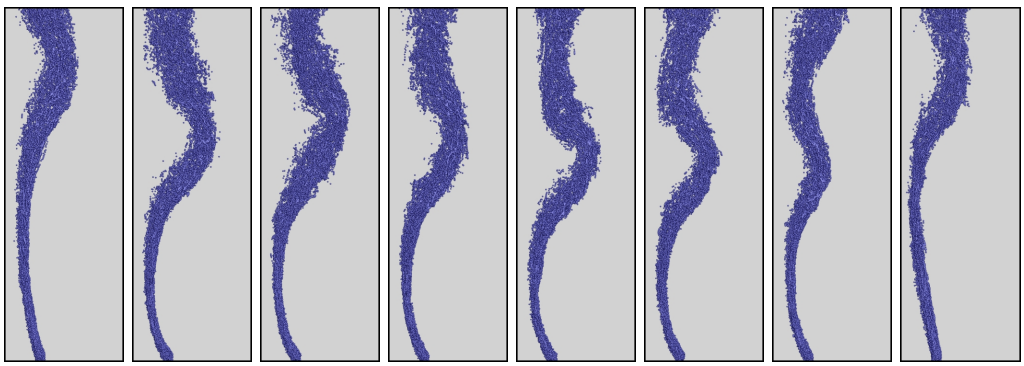

(a) (b) (c) (d) (e) (f) (g) (h)

Figure 24: Periodic migration of the bubble swarm. Each figure is a snapshot of instantaneous bubble positions, with 7 seconds between each frame. The first (a) and last (h) frame are chosen to correspond with the approximate beginning and end of one cycle.

Copyright © 2010 John Wiley & Sons, Ltd.
Prepared using fldauth.cls

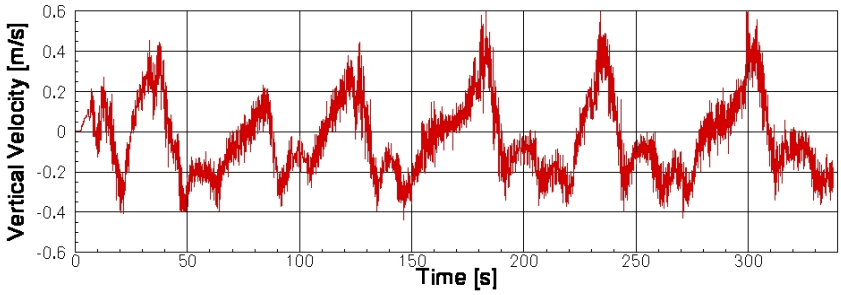

(a) Point 'A' vertical velocity

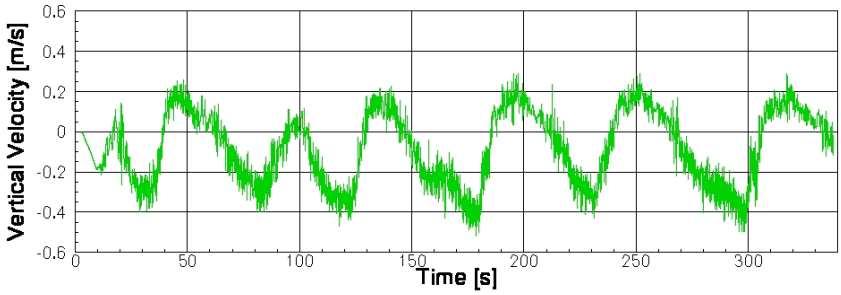

(b) Point 'B' vertical velocity

Figure 25: Fluid velocity at the points 'A' and 'B' shown in Figure 23a.

seconds longer than observed in the experiments. Deen et al. [13] and [14] also had trouble matching the oscillation period in their computations. There are numerous factors which play a role in the oscillation period including grid resolution, bubble size, lift coefficient and drag coefficient. Also it was found that small changes in the injection velocity and inlet conditions can influence the oscillation periods. The LES results with volumetric coupling; however, do show the experimentally observed trends of periodic jet oscillation and large scale vortical regions.

6. SUMMARY AND CONCLUSIONS

In this work a numerical approach capable of capturing the bubble dynamics of subgrid (or under-resolved) bubbles was developed. A mixture-theory based Eulerian-Lagrangian approach accounting for volumetric displacements due to bubble motion and size variations was implemented into an unstructured grid large-eddy simulation (LES) solver [39]. The bubble dynamics is modeled by Rayleigh-Plesset equations using an adaptive time-stepping scheme. A generalized criterion based on the eigenvalues of the coupled ordinary differential equations for bubble radius was developed and tested to give robust solutions for large variations in the surrounding pressure field. A detailed verification and validation study of this approach was performed to test the accuracy of the method on a variety of single and multiple bubble problems to show good predictive capability. The approach was applied to study bubble-vortex interaction in a traveling vortex tube (a two-dimensional representation of a vortex

Copyright © 2010 John Wiley & Sons, Ltd.

Prepared using fldauth.cls

ring experiment by Sridhar and Katz [55]) and small-scale cavitation and inception in a high-speed flow over an open cavity [37]. It was found that the Eulerian-Lagrangian subgrid model captures the trends observed in the experiments. The above numerical approach is developed in a parallel numerical framework [5] for large-scale simulations of bubbly flows. The approach is suitable for simulation of subgrid bubble dynamics in complex flows without cavitation as well small-scale bubbly cavitating flows. Use of unstructured grids facilitates application of the numerical approach to complex configurations.

The approach is suitable for simulation of up to million bubbles in a turbulent flow. Large number of bubbles with non-uniform distribution; however, can lead to presence of bubbles on only few number of processors partaking in the simulation. This gives rise to load imbalance, especially if the computational domain is partitioned based on the background mesh. Dual-constraint partitioning that optimize the number of grid cells and the number of Lagrangian points are necessary to balance the load and improve the efficiency of the scheme. These dynamic-load balancing strategies together with advanced methods for finding the nearest neighbors within the mollification kernels will make the current approach feasible for full three-dimensional simulations [49].

ACKNOWLEDGEMENT

This work is supported in part by the Office of Naval Research grant number N000140610697 monitored by Dr. Ki-Han Kim and the Department of Energy's NETL-URS Grant Number 41817M4077. SVA also acknowledges summer support under DoE's ORISE faculty summer research participation program. We acknowledge the computing time on TACC's Lonestar computing facility for the LES study of flow over an open cavity.

REFERENCES

1. H. Alehossein and Z. Qin. Numerical analysis of Rayleigh–Plesset equation for cavitating water jets. *Int. J. Numer. Meth. Eng.*, 72(7):780 – 807, March 2007.
2. MP Allen and DJ Tildesley. *Computer simulation of liquids*. Oxford University Press, USA, 1990.
3. MJ Andrews and PJ O'Rourke. The multiphase particle-in-cell (mp-pic) method for dense particulate flows. *Int. J. Multiphase Flow*, 22(2):379–402, 1996.
4. S. V. Apte, M. Gorokhovski, and P. Moin. Les of atomizing spray with stochastic modeling of secondary breakup. *Int. J. Multiphase Flow*, 29(9):1503–1522, 2003.
5. S. V. Apte, K. Mahesh, P. Moin, and J. C. Oefelein. Large-eddy simulation of swirling particle-laden flows in a coaxial-jet combustor. *Int. J. Multiphase Flow*, 29(8):1311–1331, 2003.
6. S. Becker, A. Sokolichin, and G. Eigenberger. Gas-liquid flow in bubble columns and loop reactors. II: Comparison of detailed experiments and flow simulations. *Chem. Engng. Sci.*, 49(24 B):5747–5762, 1994.
7. Christofer Earls Brennen. *Cavitation and Bubble Dynamics*. Oxford University Press New York, 1995.
8. GL Chahine, E. Delepoule, and P. Hauwaert. Study of the interaction between a bubble and a vortical structure. *ASME-PUBLICATIONS-FED*, 153:39–39, 1993.
9. PA Cundall and ODL Strack. A discrete numerical model for granular assemblies. *Geotechnique*, 29(1):47–65, 1979.
10. D. Darmana, N. G. Deen, and J. A. M. Kuipers. Parallelization of an euler-lagrange model using mixed domain decomposition and a mirror domain technique: Application to dispersed gas-liquid two-phase flow. *J. Comput. Phys.*, 220(1):216–248, 2006.
11. D. Darmana, NG Deen, and JAM Kuipers. Parallelization of an Euler–Lagrange model using mixed domain decomposition and a mirror domain technique: Application to dispersed gas–liquid two-phase flow. *J. Comput. Phys.*, 220(1):216–248, 2006.
12. N. G. Deen, M. van Sint Annaland, and J. A. M. Kuipers. Multi-scale modeling of dispersed gas-liquid two-phase flow. *Chem. Engng. Sci.*, 59(8-9):1853 – 1861, 2004. Complex Systems and Multi-scale Methodology.

Copyright © 2010 John Wiley & Sons, Ltd.

Prepared using fldauth.cls

13. NG Deen, T. Solberg, and BH Hjertager. Numerical Simulation of the Gas-Liquid Flow in a Square Cross-sectioned Bubble Column. In *14th Int. Congress of Chemical and Process Engineering. Praha-Czech Republic*. Citeseer, 2000.
14. E. Delnoij, FA Lammers, JAM Kuipers, and WPM Van Swaaij. Dynamic simulation of dispersed gas-liquid two-phase flow using a discrete bubble model. *Chem. Engng. Sci.*, 52(9):1429–1458, 1997.
15. John K. Dukowicz. A particle-fluid numerical model for liquid sprays. *J. Comput. Phys.*, 35(2):229–253, 1980.
16. J.D. Eldredge, A. Leonard, and T. Colonius. A general deterministic treatment of derivatives in particle methods. *J. Comput. Phys.*, 180(2):686–709, 2002.
17. S. Elghobashi. On predicting particle-laden turbulent flows. *Applied Scientific Research*, 52(4):309–329, 1994.
18. A. Ferrante and S.E. Elghobashi. On the effects of microbubbles on taylor–green vortex flow. *J. Fluid Mech.*, 572:145–177, 2007.
19. Antonino Ferrante and Said Elghobashi. On the accuracy of the two-fluid formulation in direct numerical simulation of bubble-laden turbulent boundary layers. *Phys. Fluids*, 19(4):045105–8, 04 2007.
20. Massimo Germano, Ugo Piomelli, Parviz Moin, and William H. Cabot. A dynamic subgrid-scale eddy viscosity model. *Phys. Fluids*, 3(7):1760–1765, 07 1991.
21. D. Gidaspow. *Multiphase Flow and Fluidization: Continuum and Kinetic Theory Descriptions*. Academic Press, 1994.
22. R.W. Hockney and J.W. Eastwood. *Computer simulation using particles*. Taylor & Francis, 1988.
23. Chao-Tsung Hsiao, Georges L. Chahine, and Han-Lieh Liu. Scaling effect on prediction of cavitation inception in a line vortex flow. *J. Fluids Eng.*, 125(1):53–60, 2003.
24. CT Hsiao and GL Chahine. Prediction of Vortex Cavitation Inception Using Coupled Spherical and Non-Spherical Models and UnRANS Computations. 2002.
25. CT Hsiao, A. Jain, and G. Chahine. Effect of Gas Diffusion on Bubble Entrainment and Dynamics around a Propeller. In *Proceedings of 26th Symp. Naval Hydrodynamics, Rome, Italy*, volume 26, 2006.
26. G. Hu and I. Celik. Eulerian–Lagrangian based large-eddy simulation of a partially aerated flat bubble column. *Chem. Engng. Sci.*, 63(1):253–271, 2008.
27. K. Hutter and K. Jöhnk. *Continuum methods of physical modeling*. Springer, 2004.
28. R. Jackson. Locally averaged equations of motion for a mixture of identical spherical particles and a newtonian fluid. *Chem. Engng. Sci.*, 52(15):2457–2469, 8 1997.
29. H. Jang and K. Mahesh. Large Eddy Simulation of Ducted Propulsors in Crashback. In *27th Symposium on Naval Hydrodynamics, Seoul, Korea*, 2008.
30. VE Johnson and T. Hsieh. The Influence of the Trajectories of Gas Nuclei on Cavitation Inception. *Sixth Symp. Naval Hydrodynamics*, pages 163–179, 1966.
31. D. D. Joseph, T. S. Lundgren, R. Jackson, and D. A. Saville. Ensemble averaged and mixture theory equations for incompressible fluid–particle suspensions. *Int. J. Multiphase Flow*, 16(1):35–42, 1990/2// 1990.
32. G. Karypis and V. Kumar. A fast and high quality multilevel scheme for partitioning irregular graphs. *SIAM Journal on Scientific Computing*, 20(1):359, 1999.
33. Dongjoo Kim and Haecheon Choi. A second-order time-accurate finite volume method for unsteady incompressible flow on hybrid unstructured grids. *J. Comput. Phys.*, 162(2):411–428, 8 2000.
34. Atsuhide Kitagawa, Yuichi Murai, and Fujio Yamamoto. Two-way coupling of eulerian-lagrangian model for dispersed multiphase flows using filtering functions. *Int. J. Multiphase Flow*, 27(12):2129–2153, 2001.
35. J. A. M. Kuipers, K. J. van Duin, F. P. H. van Beckum, and W. P. M. van Swaaij. Computer simulation of the hydrodynamics of a two-dimensional gas-fluidized bed. *Computers & Chemical Engineering*, 17(8):839–858, 8 1993.
36. G. Li and M.F. Modest. An effective particle tracing scheme on structured/unstructured grids in hybrid finite volume/PDF Monte Carlo methods. *Journal of Computational Physics*, 173(1):187–207, 2001.
37. Xiaofeng Liu and Joseph Katz. Cavitation phenomena occurring due to interaction of shear layer vortices with the trailing corner of a two-dimensional open cavity. *Phys. Fluids*, 20(4), 2008.
38. R. L
"ohner. *Applied computational fluid dynamics techniques: an introduction based on finite element methods*. Wiley, 2008.
39. K. Mahesh, G. Constantinescu, S. Apte, G. Iaccarino, F. Ham, and P. Moin. Large-eddy simulation of reacting turbulent flows in complex geometries. *J. Appl. Mech*, 73:374, 2006.
40. K. Mahesh, G. Constantinescu, and P. Moin. A numerical method for large-eddy simulation in complex geometries. *J. Comput. Phys.*, 197(1):215–240, 2004.
41. R. McDermott and S. B. Pope. The parabolic edge reconstruction method (perm) for lagrangian particle advection. *J. Comput. Phys.*, 227(11):5447–5491, 2008.
42. P. Moin. *Fundamentals of Engineering Numerical Analysis*. Cambridge University Press, 2001.

Copyright © 2010 John Wiley & Sons, Ltd.

Prepared using fldauth.cls

43. P. Moin and SV Apte. Large-Eddy Simulation of Realistic Gas Turbine-Combustors. *AIAA Journal*, 44(4):698–708, 2006.
44. P. Moin, K. Squires, W. Cabot, and S. Lee. A dynamic subgrid-scale model for compressible turbulence and scalar transport. *Phys. Fluids*, 3(11):2746–2757, 11 1991.
45. R.L. Panton. *Incompressible Flow*. Wiley-Interscience, 2006.
46. C.D. Pierce and P. Moin. Large eddy simulation of a confined coaxial jet with swirl and heat release. In *AIAA, Fluid Dynamics Conference, 29 th, Albuquerque, NM*, 1998.
47. Charles D. Pierce and Parviz Moin. Progress-variable approach for large-eddy simulation of non-premixed turbulent combustion. *J. Fluid Mech.*, 504(-1):73–97, 2004.
48. M.S. Plesset and A. Prosperetti. Bubble dynamics and cavitation. *Annu. Rev. Fluid Mech.*, 9(1):145–185, 1977.
49. I. F. Sbalzarini, J. H. Walther, M. Bergdorf, S. E. Hieber, E. M. Kotsalis, and P. Koumoutsakos. Ppm - a highly efficient parallel particle-mesh library for the simulation of continuum systems. *J. Comput. Phys.*, 215(2):566–588, 7 2006.
50. D. M. Snider. An incompressible three-dimensional multiphase particle-in-cell model for dense particle flows. *J. Comput. Phys.*, 170(2):523–549, 2001.
51. S. Sobhani et al. *Numerical simulation of cavitating bubble-laden turbulent flows*. PhD thesis, Oregon State University, 2010.
52. A. Sokolichin and G. Eigenberger. Applicability of the standard k–ε turbulence model to the dynamic simulation of bubble columns: Part I. Detailed numerical simulations. *Chem. Engng. Sci.*, 54(13-14):2273–2284, 1999.
53. M. Sommerfeld, E. Bourloutski, and D. Broder. Euler/Lagrange Calculations of Bubbly Flows with Consideration of Bubble Coalescence. *Canadian J. Chem. Engng.*, 81(3/4):508–518, 2003.
54. G. Sridhar and J. Katz. Drag and lift forces on microscopic bubbles entrained by a vortex. *Phys. Fluids*, 7(2):389–399, 02 1995.
55. G. Sridhar and J. Katz. Effect of entrained bubbles on the structure of vortex rings. *J. Fluid Mech.*, 397(-1):171–202, 1999.
56. Y. Tsuji, T. Kawaguchi, and T. Tanaka. Discrete particle simulation of two-dimensional fluidized bed. *Powder technology*, 77(1):79–87, 1993.
57. M.A. van der Hoef, M. van Sint Annaland, N.G. Deen, and J.A.M. Kuipers. Numerical simulation of dense gas-solid fluidized beds: A multiscale modeling strategy. *Annu. Rev. Fluid Mech.*, 40(1):47–70, 2008.
58. M. van Sint Annaland, N. G. Deen, and J. A. M. Kuipers. Numerical simulation of gas bubbles behaviour using a three-dimensional volume of fluid method. *Chemical Engineering Science*, 60(11):2999–3011, 6 2005.
59. T. Westermann. Localization schemes in 2D boundary-fitted grids. *Journal of Computational Physics*, 101(2):307–313, 1992.
60. D. Z. Zhang and A. Prosperetti. Ensemble phase-averaged equations for bubbly flows. *Physics of Fluids*, 6(9):2956–2970, 1994.

APPENDIX

Search Algorithm for Locating Bubbles:

In Euler-Lagrange simulations, it is necessary to locate the bubble/particle onto a background grid as it moves from one location to another. This involves two parts: (i) strategy to decide whether a bubble lies inside a grid control volume, and (ii) effectively locating the bubble by applying the bubble-locating strategy to few number of control volumes.

Bubble/Particle Location Strategy: Locating particles in a generalized-coordinate structured code is straightforward since the physical coordinates can be transformed into a uniform computational space. This is not the case for unstructured grids. Westermann [59] describes several approaches to locate particles in particle-in-cell codes. Two such techniques are described below.

One approach to determine whether a particle lies inside a control volume is based on the calculation of partial volumes. The nodes of the control volume are joined to the particle

Copyright © 2010 John Wiley & Sons, Ltd.

Prepared using fldauth.cls

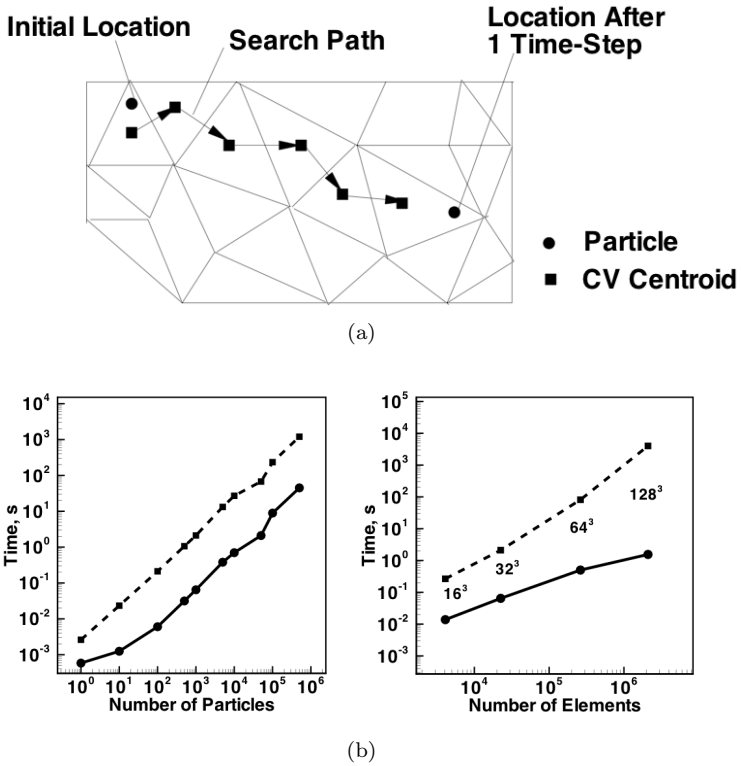

Figure 26: (*a*) Schematic of the known-vicinity algorithm to track particle positions on unstructured grids. (*b*) Comparison of the modified brute force and known vicinity search algorithms, —— known-vicinity, - - - - modified brute force.

location, and the volumes of the resulting sub-cells are compared to that of the control volume. If the particle lies inside the control volume, the sum of the sub-cell volumes will be equal to the total volume. However, this approach was found to fail drastically for highly skewed meshes due to round-off inaccuracies in the computation of partial volumes.

The second approach projects the particle location onto the faces of the control volume and compares these vectors with outward face-normals for all faces. If the particle lies within the cell, the projected vectors point the same way as the outward face-normals. This technique is found to be very accurate even for highly skewed elements. A search algorithm is then required to efficiently select the control volume to which the criterion should be applied.

Search Algorithm: Two approaches were examined and are termed as the modified brute-force and known-vicinity algorithms, respectively. A naive strategy (brute-force approach) would simply loop over all the elements of the grid and applies the localization criterion described above. As expected, it is extremely slow for a large number of particles, as is the case even for coarse LES. The modified brute-force approach evaluates the closest point of the mesh to the particle location and only considers the elements surrounding that point. Should this attempt (which in general is very successful) fail, the elements surrounding all the close

Copyright © 2010 John Wiley & Sons, Ltd.

Prepared using fldauth.cls

points are considered. If this also fails for some pathological cases [38], the search region is enlarged or the brute force method is applied. This modified approach is found effective to initialize particles, and as a fall-back position for more refined algorithms.

Given a good initial guess for a particle location, the known-vicinity algorithm out performs all others [38]. Particle location at earlier time-steps provide a very good initial guess in LES. Knowing the initial and final location of the particle, this algorithm searches in the direction of the particle motion until it is relocated (Fig. 26(a)). The neighbor-to-neighbor search is extremely efficient if the particle is located within 10-15 attempts, which is usually the case for 95% of the particles in present simulations. If this algorithm fails, we fall-back to the 'modified-brute force' method to locate the particle. A combination of these two algorithms is found highly efficient and robust for complex geometries and hybrid meshes encountered in realistic combustor geometries. A similar approach was also applied by Li & Modest [36] to perform hybrid finite volume/PDF-Monte Carlo simulations implying a wide range of potential applications utilizing this scheme.

The known-vicinity algorithm is compared to the modified-brute force method in Fig. 26(b). Two cases are considered: (i) the grid is fixed, and the particles are displaced by 2-3 cell-sizes in all three coordinate directions, (ii) the number of particles is fixed (~ 1000) and the number of elements per processor is increased. The known-vicinity approach is seen to be noticeably better than the modified brute-force. Note that these comparisons were performed on a single processor of an Origin 2000 for a cubic box with tetrahedral elements.

Copyright © 2010 John Wiley & Sons, Ltd.

Prepared using fldauth.cls